Probing right handed neutrinos at the LHeC and lepton colliders using fat jet signatures

Arindam Das,[1,*] Sudip Jana,[2,†] Sanjoy Mandal,[3,4,‡] and S. Nandi[2,§]

[1]School of Physics, KIAS, Seoul 02455, Korea
[2]Department of Physics and Oklahoma Center for High Energy Physics, Oklahoma State University, Stillwater, Oklahoma 74078-3072, USA
[3]The Institute of Mathematical Sciences, C.I.T Campus, Taramani, Chennai 600 113, India
[4]Homi Bhabha National Institute, BARC Training School Complex, Anushakti Nagar, Mumbai 400085, India

(Received 20 November 2018; published 25 March 2019)

The inclusion of heavy neutral leptons (right-handed neutrinos) to the Standard Model (SM) particle content is one of the best motivated ways to account for the observed neutrino masses and flavor mixing. The modification of the charged and neutral currents from active-sterile mixing of the neutral leptons can provide novel signatures which can be tested at the future collider experiments. In this article, we explore the discovery prospect of a very heavy right handed neutrino to probe such extensions at the future collider experiments like Large Hadron electron Collider (LHeC) and linear collider. We consider the production of the heavy neutrino via the t and s-channel processes and its subsequent decays into the semileptonic final states. We specifically focus on the scenario where the gauge boson produced from heavy neutrino decay is highly boosted, leading to a fat jet. We study the bounds on the sterile neutrino properties from several past experiments and compare with our results.

DOI: 10.1103/PhysRevD.99.055030

I. INTRODUCTION

One of the most robust evidence that points out to an important inadequacy of the SM is the existence of the tiny but nonzero neutrino masses. It seems unlikely that the very small neutrino masses are generated by the same Higgs mechanism responsible for the masses of the other SM fermions due to the absence of right-handed neutrinos. Even then, extremely small Yukawa couplings, of the order of $\lesssim 10^{-12}$, must be invoked. There are various BSM extensions which have been proposed to explain small neutrino masses. Among those, one of the most appealing framework of light neutrino mass generation is the addition of new states that, once integrated out, generate the lepton number violating dimension five Weinberg operator $\mathcal{O}_5 = \frac{c}{\Lambda} LLHH$ [1]. This is embodied by the so-called seesaw mechanisms. There can be a few different variations of seesaw, Type-I [2], Type-II [3], Type-III [4], inverse [5] and radiative [6] seesaw.

Most of the UV completed seesaw models contain Standard Model (SM) gauge singlet heavy right handed neutrino N. Through the seesaw mechanism, the Majorana type right handed neutrinos (RHNs) impart masses to the SM light neutrinos and hence establishes the fact that SM neutrinos have masses which have been experimentally observed in a several neutrino oscillation experiments [7]. These RHNs can have masses from eV scale to 10^{14} GeV scale depending upon the models. For instance, the sterile neutrinos [8] with masses in the eV range could lead to effects in short distance neutrino oscillation experiments by introducing an additional mass squared difference, keV mass sterile neutrinos are potential candidates for "warm" dark matter, MeV scale sterile neutrinos can be possible explanation for MiniBoone [9] and there can be very heavy sterile neutrinos with masses $M_{\rm GUT} \sim 10^{14}$ GeV, close to $M_{\rm GUT} \sim 10^{16}$ GeV in model of grand unified theories (GUTs). These RHNs, originally Standard Model (SM) gauge singlet, being mixed with the SM light neutrinos to interact with the SM gauge bosons. Depending on the mass of the gauge singlet RHNs and their mixings with the active neutrino states, seesaw mechanism can be tested at colliders [10–52], as well as, in other noncollider experiments, such as, neutrinoless double beta decay [26,53–59], neutrino experiments [8,9,60], rare-meson decays [61–63], muon $g-2$ [64], lepton flavor violating processes $l_i \to l_j\gamma$, $\mu \to 3e$, $\mu \to e$ conversion in nuclei [65–67], nonunitarity [68–72], etc.

*arindam@kias.re.kr
†sudip.jana@okstate.edu
‡smandal@imsc.res.in
§s.nandi@okstate.edu

We are specifically interested in the RHNs at the TeV scale so that they can be tested at the high energy colliders. At the LHC, the production cross section of the RHN decreases as the mass of RHN increases as a result of the properties of the constituent quarks of the proton beams. In the linear collider the electron and positron are collided to produce the RHN in association with a light neutrino through the dominant t-channel process. A subdominant s-channel process also contributes [73,74]. Otherwise a variety of RHN productions at the linear collider have been discussed in [75] followed by the bounds on the light heavy mixing angles for the electron flavor at the linear collider with 500 GeV and 1 TeV collider energies. The low mass range of the RHN has been studied in [76] which also predicts the limit on the light heavy mixing and the mass of the RHN up to a mass of 250 GeV. The sterile neutrinos at the circular lepton colliders have been studied in [77] which deals with a comprehensive discussion on the detectors from experimental point of view. Higgs searches from RHN has been studied in [78] where the RHN has been produced from the W and Z mediated processes. Such a RHN decays into a Higgs and SM light neutrino and the Higgs can dominantly decay into a pair of b-quarks. Hence a $2b$ plus missing momentum will be a signal from this process. In this paper the RHN up to a 500 GeV mass have been tested where the maximum center of mass energy is also taken up to 500 GeV. The distinct and interesting signature of the RHN can be displaced vertex search if the mixing between the light and heavy neutrinos become extremely small. Such a scenario has been tested in [79] for the colliders 240 GeV, 350 GeV and 500 GeV. Another interesting work on the RHNs has been found in the form of [80] where a variety of the colliders have been considered to test the observability of the RHN production. They have discussed several production modes of the RHNs at the LHC, lepton-hadron collider (LHeC)[1] [87] and linear collider. They have studied all possible modes of the RHN production in these colliders and compared the bounds on the light-heavy neutrino mixing angles. In the linear collider, the references [76–80] did not go further than 500 GeV as they constrained themselves within the center of mass energy of 500 GeV. However, none of these papers studied the boosted object at the LHeC and linear collider respectively.

In our analysis we consider the following things:

(1) We study the prospect of discovery of RHNs at LHeC considering the boosted objects for the first time. In the LHeC we concentrate on the lepton number violating (LNV) and lepton number conserving (LNC) channels to produce the RHN in association with a jet (j_1). Hence the RHN will decay into the dominant ℓW and the W will decay into a pair of jets. The daughter W coming from the heavy RHN will be boosted and its hadronic decay products, jets, of the W will be collimated such that they can form a fat jet (J).Hence a signal sample of $\ell + j_1 + J$ can be studied thoroughly at this collider. In this process people have mostly studied the lepton number conserving channel where as the lepton number violating will be potentially background free. However, for clarity we study the combined channel and the corresponding SM backgrounds. We consider two scenarios at the LHeC where the electron and proton beams will have 60 GeV and 7 TeV energies where the center of mass energy becomes $\sqrt{s} = 1.3$ TeV. We have also considered another center of mass energy at the $\sqrt{s} = 1.8$ TeV where the proton beam energy is raised up to the 13.5 TeV. For both of the colliders we consider the luminosity at 1 ab^{-1}. Here the RHN is a first generation RHN (N_1) and ℓ is electron (e). Finally we study up to 3 ab^{-1} luminosity.

(2) At the linear collider the production of the RHNs is occurring from the s- and t- channel processes in association with a SM light neutrino (ν). We consider the linear collider at two different center of mass energies, such as $\sqrt{s} = 1$ TeV and $\sqrt{s} = 3$ TeV which can probe up to a high mass of the RHNs such as 900 GeV (at the 1 TeV linear collider) and 2.9 TeV (at the 3 TeV linear collider) due to the almost constant cross section for the $N\nu$ production. For both of the center of mass energies we consider 1 ab^{-1} luminosity. Finally we study up to 3(5) ab^{-1} luminosity for the 1 (3) TeV linear collider.

At this mass scale, the RHNs will be produced at rest, however, the daughter particles can be sufficiently boosted. We consider $N \to \ell W$, $W \to jj$ and $N \to h\nu$, $h \to b\bar{b}$ modes at the linear collider where h is the SM Higgs boson. If the RHN is sufficiently heavy, such the, $M_N \geq 400$ GeV, the W and h can be boosted because M_W and $M_h \ll \frac{M_N}{2}$. As a result W and h will produce a fat jet (J) and a fat b jet (J_b), respectively. Therefore the signal will be $\ell + J$ plus missing momentum and J_b plus missing momentum in the W and h modes, respectively, at the linear collider. Therefore studying the signals and the backgrounds for each process we put the bounds in the mass- mixing plane of the RHNs.

(3) We want to comment that studying $e^-e^+ \to N_2\nu_\mu/N_3\nu_\tau$ mode in the Z mediated s-channel will be interesting where $N_2(N_3)$ will be the second (third) generation RHN. Studying the signal events and the corresponding SM backgrounds one can also calculate the limits on the mixing angles involved in these processes. Such a process will be proportional to $|V_{\mu N}|^2(|V_{\tau N}|^2)$. In these processes the signal will

[1]In such a collider we can also nicely study the long lived particles in [81], beyond the SM physics in [82], leptoquarks [83], left-right model [84], charged Higgs [85] and heavy Majorana neutrinos [86]. The LHeC design report can be found in [83].

be $\mu(\tau)+jj$ plus missing momentum followed by the decay of $N_2(N_3)\to\mu jj(\tau jj)$. One can also calculate the bounds on the mass-mixing plane for different significances. A boosted analysis could be interesting, however, a nonboosted study might be more useful as the cross section goes down with the rise in collider energy in these processes. Such signals can also be studied if the RHNs can decay through the LFV modes, such as $e^-e^+\to N\nu_e$, $N\to\mu W$, $W\to jj$, however, $\mu\to e\gamma$ process will make this process highly constrained due to the strong limit $\mathrm{Br}(\mu^+\to e^+\gamma)<4.2\times10^{-13}$ at the 90% C. L. [88]. The corresponding limits on τ are weaker [89,90]. Such final states have been studied in [73] for $M_N=150$ GeV, a high mass test with using boosted object will be interesting in the future. A comprehensive LHC study has been performed in [91].

(4) The RHN produced at the linear collider may decay in to another interesting mode, namely, $N\to Z\nu$, $Z\to b\bar{b}$, which can be another interesting channel where boosted objects can be stated. However, precision measurements at the Z-boson resonance using electron-positron colliding beams at LEP experiment strongly constrains Z boson current, and hence, $Zb\bar{b}$ coupling. This channel also suffers from larger QCD background compared to the leptonic decay of Z boson, and hence, leptonic decay of Z boson has a better discovery prospect for this particular mode of RHN decay. On the other hand, SM Higgs, h, mostly decays (∼60%) to $b\bar{b}$ due to large $hb\bar{b}$ coupling. Due to this, we focus on the Higgs decay mode of RHN, $N\to h\nu$, $h\to b\bar{b}$ to study the fat jet signature. For the time being, we mainly focus on the first two items. The investigation of the mode, $N\to Z\nu$, $Z\to b\bar{b}$ is beyond the scope of this article and shall be presented in future work in detail.

The paper is organized as follows. in Sec. II, we discuss the model and the interactions of the heavy neutrino with SM particles and also calculate the production cross sections at different colliders. In Sec. III we discuss the complete collider study. In Sec. IV we calculate the bounds on the mixing angles and compare them with the existing results. Finally, we conclude in Sec. V.

II. MODEL AND THE PRODUCTION MODE

In type-I seesaw [2], SM gauge-singlet right handed Majorana neutrinos N_R^β are introduced, where β is the flavor index. N_R^β have direct coupling with SM lepton doublets ℓ_L^α and the SM Higgs doublet H. The relevant part of the Lagrangian can be written as:

$$\mathcal{L}\supset -Y_D^{\alpha\beta}\overline{\ell_L^\alpha}HN_R^\beta-\frac{1}{2}M_N^{\alpha\beta}\overline{N_R^{\alpha C}}N_R^\beta+\mathrm{H.c.} \tag{1}$$

After the spontaneous EW symmetry breaking by getting the vacuum expectation value (VEV) of the Higgs field, $H=\binom{\frac{v}{\sqrt{2}}}{0}$, we obtain the Dirac mass matrix as $M_D=\frac{Y_D v}{\sqrt{2}}$. Using the Dirac and Majorana mass matrices, the neutrino mass matrix can be written as

$$M_\nu=\begin{pmatrix}0 & M_D\\ M_D^T & M_N\end{pmatrix}. \tag{2}$$

After diagonalizing this matrix, we obtain the seesaw formula for the light Majorana neutrinos as

$$m_\nu\simeq -M_D M_N^{-1}M_D^T. \tag{3}$$

For $M_N\sim100$ GeV, we may find $Y_D\sim10^{-6}$ with $m_\nu\sim0.1$ eV. However, in the general parametrization for the seesaw formula [92], Dirac Yukawa term Y_D can be as large as 1, and this scenario is considered in this paper.

There is another seesaw mechanism, so-called inverse seesaw [5], where the light Majorana neutrino mass is generated through tiny lepton number violation. The relevant part of the Lagrangian is given by

$$\mathcal{L}\supset -Y_D^{\alpha\beta}\overline{\ell_L^\alpha}HN_R^\beta-M_N^{\alpha\beta}\overline{S_L^\alpha}N_R^\beta-\frac{1}{2}\mu_{\alpha\beta}\overline{S_L^\alpha}S_L^{\beta C}+\mathrm{H.c.}, \tag{4}$$

where M_N is the Dirac mass matrix, N_R^α and S_L^β are two SM-singlet heavy neutrinos with the same lepton numbers, and μ is a small lepton number violating Majorana mass matrix. After the electroweak symmetry breaking the neutrino mass matrix is obtained as

$$M_\nu=\begin{pmatrix}0 & M_D & 0\\ M_D^T & 0 & M_N^T\\ 0 & M_N & \mu\end{pmatrix}. \tag{5}$$

After diagonalizing this mass matrix, we obtain the light neutrino mass matrix

$$M_\nu\simeq M_D M_N^{-1}\mu M_N^{-1^T}M_D^T. \tag{6}$$

Note that the small lepton number violating term μ is responsible for the tiny neutrino mass generation. The smallness of μ allows the $M_D M_N^{-1}$ parameter to be order one even for an EW scale heavy neutrino. Since the scale of μ is much smaller than the scale of M_N, the heavy neutrinos become the pseudo-Dirac particles. This is the main difference between the type-I and the inverse seesaw.

Assuming $M_D M_N^{-1}\ll1$, the flavor eigenstates (ν) of the light Majorana neutrinos can be expressed in terms of the mass eigenstates of the light (ν_m) and heavy (N_m) Majorana neutrinos such as

$$\nu\simeq\mathcal{N}\nu_m+\mathcal{R}N_m, \tag{7}$$

where

$$\mathcal{R} = M_D M_N^{-1}, \qquad \mathcal{N} = \left(1 - \frac{1}{2}\epsilon\right) U_{\rm MNS} \tag{8}$$

with $\epsilon = \mathcal{R}^* \mathcal{R}^T$, and U_{MNS} is the usual neutrino mixing matrix by which the mass matrix m_ν is diagonalized as

$$U_{MNS}^T m_\nu U_{MNS} = \text{diag}(m_1, m_2, m_3). \tag{9}$$

In the presence of ϵ, the mixing matrix $\mathcal{N}$ is not unitary [65,68,69,93]. Considering the mass eigenstates, the charged current interaction in the Standard Model is given by

$$\mathcal{L}_{CC} = -\frac{g}{\sqrt{2}} W_\mu \bar{e} \gamma^\mu P_L (\mathcal{N} \nu_m + \mathcal{R} N_m) + \text{H.c.}, \tag{10}$$

where e denotes the three generations of the charged leptons in the vector form, and $P_L = \frac{1}{2}(1 - \gamma_5)$ is the projection operator. Similarly, the neutral current interaction is given by

$$\mathcal{L}_{NC} = -\frac{g}{2c_w} Z_\mu [\overline{\nu_m} \gamma^\mu P_L (\mathcal{N}^\dagger \mathcal{N}) \nu_m + \overline{N_m} \gamma^\mu P_L (\mathcal{R}^\dagger \mathcal{R}) N_m + \{\overline{\nu_m} \gamma^\mu P_L (\mathcal{N}^\dagger \mathcal{R}) N_m + \text{H.c.}\}], \tag{11}$$

where $c_w = \cos\theta_w$ is the weak mixing angle. Because of nonunitarity of the matrix $\mathcal{N}$, $\mathcal{N}^\dagger \mathcal{N} \neq 1$ and the flavor-changing neutral current occurs.

The dominant decay modes of the heavy neutrino are $N \to \ell W$, $\nu_\ell Z$, $\nu_\ell h$ and the corresponding partial decay widths are respectively given by

$$\begin{aligned}
\Gamma(N \to \ell W) &= \frac{g^2 |V_{\ell N}|^2}{64\pi} \frac{(M_N^2 - M_W^2)^2 (M_N^2 + 2M_W^2)}{M_N^3 M_W^2}, \\
\Gamma(N \to \nu_\ell Z) &= \frac{g^2 |V_{\ell N}|^2}{128\pi c_w^2} \frac{(M_N^2 - M_Z^2)^2 (M_N^2 + 2M_Z^2)}{M_N^3 M_Z^2}, \\
\Gamma(N \to \nu_\ell h) &= \frac{|V_{\ell N}|^2 (M_N^2 - M_h^2)^2}{32\pi M_N} \left(\frac{1}{v}\right)^2.
\end{aligned} \tag{12}$$

The decay width of heavy neutrino into charged gauge bosons being twice as large as neutral one owing to the two degrees of freedom ($W^\pm$). We plot the branching ratios $\text{BR}_i (= \Gamma_i / \Gamma_{\text{total}})$ of the respective decay modes (Γ_i) with respect to the total decay width (Γ_{total}) of the heavy neutrino into W, Z and Higgs bosons in Fig. 1 as a function of the heavy neutrino mass (M_N). Note that for larger values of M_N, the branching ratios can be obtained as

$$\text{BR}(N \to \ell W) : \text{BR}(N \to \nu Z) : \text{BR}(N \to \nu H) \simeq 2 : 1 : 1. \tag{13}$$

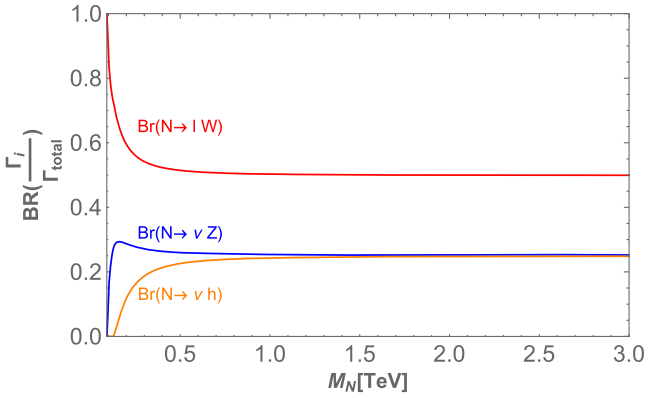

FIG. 1. Heavy neutrino branching ratios (BR_i) for different decay modes are shown with respect to the heavy neutrino mass (M_N).

A. Production cross section at LHeC

The LHeC can produce the RHN in the process $ep \to N_1 j_1$ through the t- channel exchanging the W boson. In this case the first generation RHN (N_1) will be produced. The corresponding Feynman diagram is given in Fig. 2. The total differential production cross section for this process is calculated as

$$\begin{aligned}
\frac{d\hat{\sigma}_{\rm LHeC}}{d\cos\theta} &= \frac{3.89 \times 10^8}{32\pi} 3 \times \frac{1}{3} \left(\frac{1}{2}\right)^2 \left(\frac{M_{\rm inv}^2 - M_N^2}{M_N^2}\right) \\
&\times \frac{256 C_\ell^2 C_q^2 \left(\frac{M_{inv}^2 - M_N^2}{4}\right)}{[M_N^2 - 2\{\frac{M_{\rm inv}^2}{4}(1 - \cos\theta)\} + \frac{M_{\rm inv}^2}{4}(1 + \cos\theta)]^2 + \Gamma_W^2 M_W^2}
\end{aligned} \tag{14}$$

where $C_\ell = C_q = \frac{g}{2\sqrt{2}}$. Performing the integration over $\cos\theta$ between $[-1, 1]$ we find the cross section as $\hat{\sigma}_{\rm LHeC}$ and finally convoluting the PDF (CTEQ5M) [94] we get the total cross section as

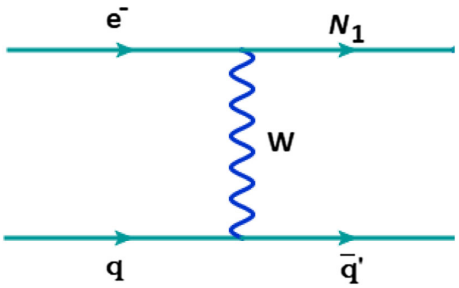

FIG. 2. Production process, $ep \to N_1 j_1$, of the RHN at the LHeC through a t channel W boson exchange.

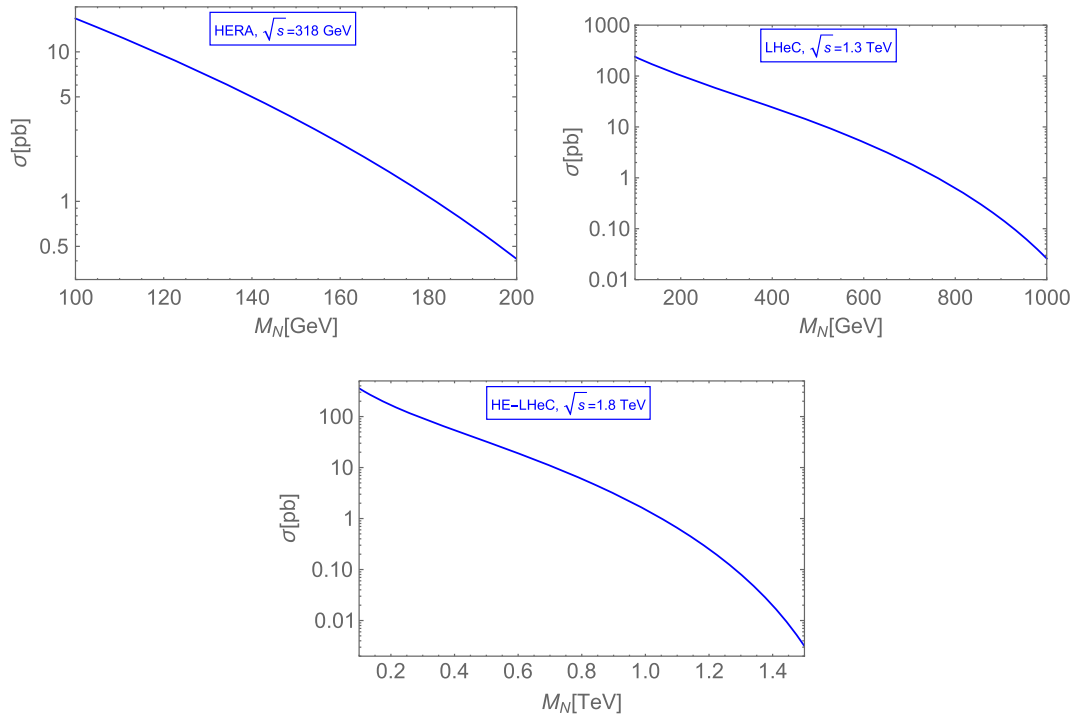

FIG. 3. RHN production cross section at the LHeC considering $ep \to N_1 j$ process for the ep collider at $\sqrt{s} = 318$ GeV (HERA, top left panel), $\sqrt{s} = 1.3$ TeV (LHeC, top right panel) and $\sqrt{s} = 1.8$ TeV (HE-LHeC, bottom panel).

$$\sigma = \sum_i \int_{\frac{M_N^2}{E_{\rm CM}^2}}^1 dx q_i(x, \sqrt{x}E_{\rm CM}) \hat{\sigma}_{\rm LHeC}(\sqrt{x}E_{\rm CM}) \tag{15}$$

where $E_{\rm CM}$ is the center of mass energy of the LHeC and i runs over the quark flavors. For different center of mass energies E will be different. In Fig. 3 we plot the total production cross sections of N_1 at the three different collider energies such as $\sqrt{s} = 318$ GeV (HERA), $\sqrt{s} = 1.3$ TeV (LHeC) and $\sqrt{s} = 1.8$ TeV (High Energy LHeC (HE-LHeC)) respectively. The cross section in Fig. 3 is normalized by the square of the mixing to correspond the maximum value for a fixed M_N according to the relevant part of the charged current interaction in Eq. (10).

B. Production cross section at linear collider

The linear collider can produce the heavy neutrino in the process $e^+e^- \to \overline{\nu_1} N_1$ through t and s-channels exchanging the W and Z bosons, respectively. The corresponding Feynman diagrams are given in Fig. 4. The total differential production cross section for this process is calculated as

$$\begin{aligned}\frac{d\sigma_{\rm ILC}}{d\cos\theta} = (3.89\times10^8\ {\rm pb})\frac{\beta}{32\pi s}\frac{s+M_N^2}{s}\left(\frac{1}{2}\right)^2\Bigg[&\frac{16C_1^2C_2^2(s^2-M_N^4)(1+\cos\theta)(1+\beta\cos\theta)}{(M_N^2-\frac{s-M_N^2}{2}(1-\beta\cos\theta)-M_W^2)^2+M_W^2\Gamma_W^2}\\ &+\frac{(4(C_{A_e}^2+C_{V_e}^2)(C_{A_\nu}^2+C_{V_\nu}^2)(1+\beta\cos^2\theta)+16C_{A_e}C_{V_e}C_{A_\nu}C_{V_\nu}(1+\beta)\cos\theta)(s^2-M_N^4)}{(s-M_Z^2)^2+M_Z^2\Gamma_Z^2}\\ &-32C_1^2C_{A_e}^2(s^2-M_N^4)(1+\cos\theta)(1+\beta\cos\theta)\\ &\times\frac{(M_N^2-\frac{s-M_N^2}{2}(1-\beta\cos\theta)-M_W^2)(s-M_Z^2)+M_WM_Z\Gamma_W\Gamma_Z}{((M_N^2-\frac{s-M_N^2}{2}(1-\beta\cos\theta)-M_W^2)^2+M_W^2\Gamma_W^2)((s-M_Z^2)^2+M_Z^2\Gamma_Z^2)}\Bigg],\end{aligned} \tag{16}$$

where $\beta = (s-M_N^2)/(s+M_N^2)$,

$$C_1 = -C_2 = \frac{g}{2\sqrt{2}}, \quad C_{A_\nu} = C_{V_\nu} = \frac{g}{4\cos\theta_W}, \quad C_{A_e} = \frac{g}{2\cos\theta_w}\left(-\frac{1}{2}+2\sin^2\theta_w\right), \quad C_{V_e} = -\frac{g}{4\cos\theta_w}. \tag{17}$$

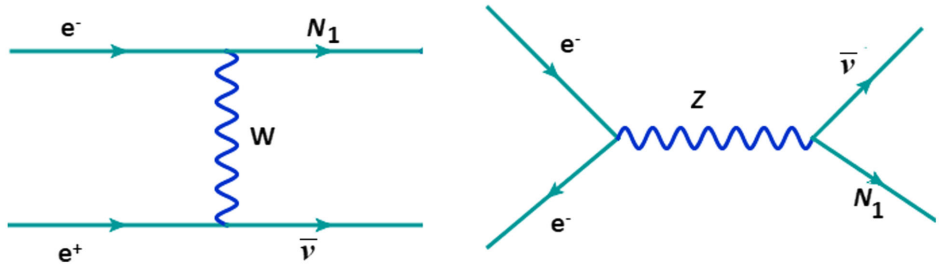

FIG. 4. RHN production processes at the linear collider. The left panel is the dominant t channel process and the right panel is s channel process to produce the $e^+e^- \to N_1\nu_1$. To produce $N_2\nu_2$ and $N_3\nu_3$, the Z mediated s channel process will act.

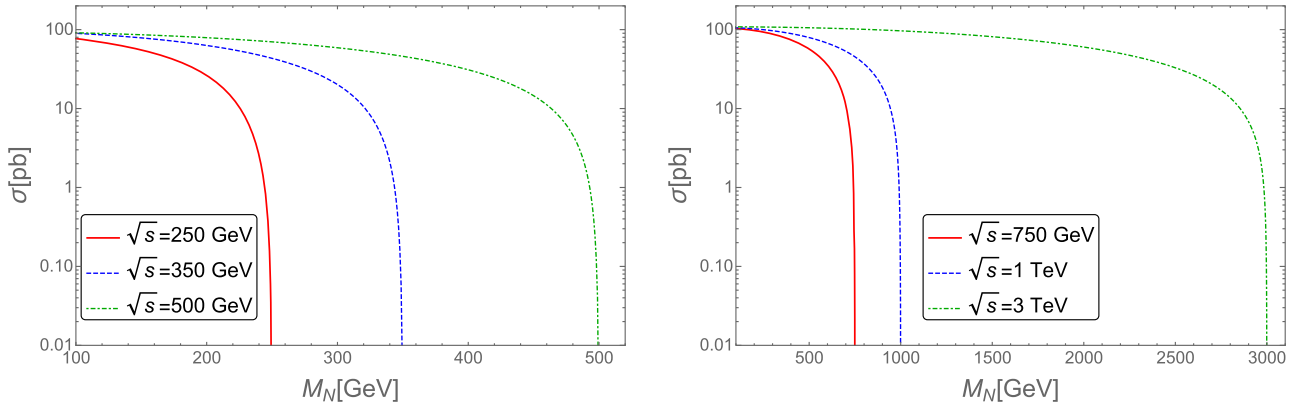

FIG. 5. RHN production cross section at the linear collider considering $e^+e^- \to N_1\nu_1$ process at the different center of mass energies.

The total production cross section for the process $e^+e^- \to \overline{\nu_1}N_1$ from the t and s channel processes at the linear collider at different center of mass energies are shown in Fig. 5.

The s channel Z mediated process can produce the second (third) generation of RHNs, $N_2(N_3)$ in association with $\nu_2(\nu_3)$. The cross sections for different center of mass energies have been given in Fig. 6. The cross section in this mode decreases with the increase in the center of mass energy. Such modes can reach up to a cross section of 1 pb for $M_N = 100$ GeV at $\sqrt{s} = 250$ GeV. Consider the leading decay mode of the RHN into W and $\ell(\mu, \tau)$ followed by the hadronic decay of the W could be interesting to probe the corresponding mixing angles. The cross sections in Figs. 5 and 6 are normalized by the square of the mixing to correspond the maximum value for a fixed M_N according to the relevant part of the charged current and neutral current interactions in Eqs. (10) and (11), respectively.

III. COLLIDER ANALYSIS

We implement our model in FeynRules [95], generate the UFO file of the model for MadGraph5-aMC@NLO

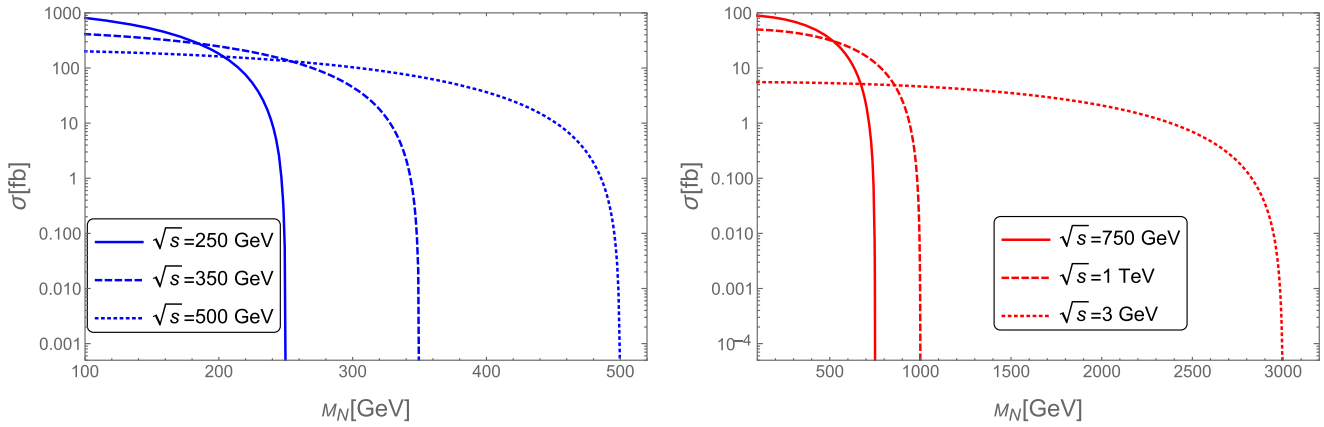

FIG. 6. RHN production cross section at the linear collider considering $e^+e^- \to N_2\nu_2(N_3\nu_3)$ process at the different center of mass energies from the s channel Z boson exchange.

[96] to calculate the signals and the backgrounds. Further we use PYTHIA6 [97] for LHeC as used in [87] and PYTHIA8 [98] for the linear colliders, where subsequent decay, initial state radiation, final state radiation and hadronization have been carried out. We have indicated in [14,15] that if the RHNs are sufficiently heavy, the daughter particles can be boosted. We prefer the hadronic decay mode of the W where the jets can be collimated so that we can call it a fat jet (J). Such a topology is very powerful to discriminate the signal from the SM backgrounds. We perform the detector simulation using DELPHES version 3.4.1 [99]. The detector card for the LHeC has been used from [100]. We use the ILD card for the linear collider. In our analysis the jets are reconstructed by Cambridge-Achen algorithm [101,102] implemented in Fastjet package [103,104] with the radius parameter as $R = 0.8$.

We study the production of the first generation RHN (N_1) and its subsequent leading decay mode ($ep \to N_1 j_1$, $N_1 \to We$, $W \to J$) at the LHeC with $\sqrt{s} = 1.3$ TeV and 1.8 TeV center of mass energies. The corresponding Feynman diagram is given in Fig. 7. We also study the RHN production at the linear collider (International Linear Collider, ILC) at $\sqrt{s} = 1$ TeV and CLIC at $\sqrt{s} = 3$ TeV collider energies. However, for simplicity we will use the term linear collider unanimously. At the linear collider we consider two sets of signals after the production of the RHN, such that, $e^+e^- \to N_1\nu$, $N_1 \to We$, $W \to J$ and $e^+e^- \to N_1\nu$, $N_1 \to h\nu$, $h \to J_b$ where J_b is a fat b-jet coming from the boosted SM Higgs decay in the dominant mode. For the two types of colliders we consider 1000 fb^{-1} luminosity. The corresponding Feynman diagrams are given in Fig. 8. For the analysis of signal and background events we use the following set of basic cuts,

(1) Electrons in the final state should have the following transverse momentum (p_T^e) and pseudorapidity ($|\eta^e|$) as $p_T^e > 10$ GeV, $|\eta^e| < 2.5$.
(2) Jets are ordered in p_T, jets should have $p_T^j > 10$ GeV and $|\eta^j| < 2.5$.
(3) Photons are counted if $p_T^\gamma > 10$ GeV and $|\eta^\gamma| < 2.5$.
(4) Leptons should be separated by $\Delta R_{\ell\ell} > 0.2$.
(5) The leptons and photons are separated by $\Delta R_{\ell\gamma} > 0.3$.
(6) The jets and leptons should be separated by $\Delta R_{\ell j} > 0.3$.
(7) Fat Jet is constructed with radius parameter $R = 0.8$.

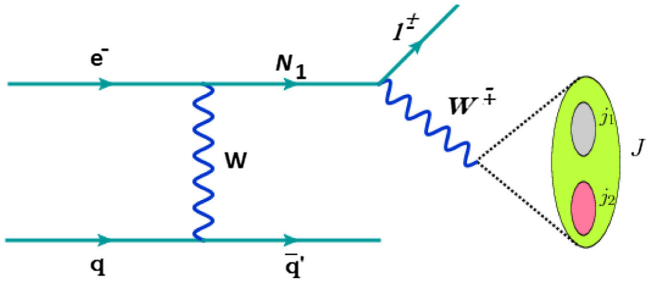

FIG. 7. $e + J + j_1$ final state at the LHeC and HE-LHeC.

A. LHeC analysis for the signal $e^-p \to jN_1 \to e^\pm + J + j_1$

Producing N_1 at the LHeC and followed by its decay into leading mode to study the boosted objects, we consider the final state $e^\pm + J + j_1$. In this case we have two different processes, one is them is the $e^+ + J + j_1$ and the other one is $e^- + J + j_1$. The first one is the lepton number violating (LNV) channel and the second one is the lepton number conserving (LNC). At the time of showing the results we combine LNV and LNC channels to obtain the final state as $e^\pm + J + j_1$.

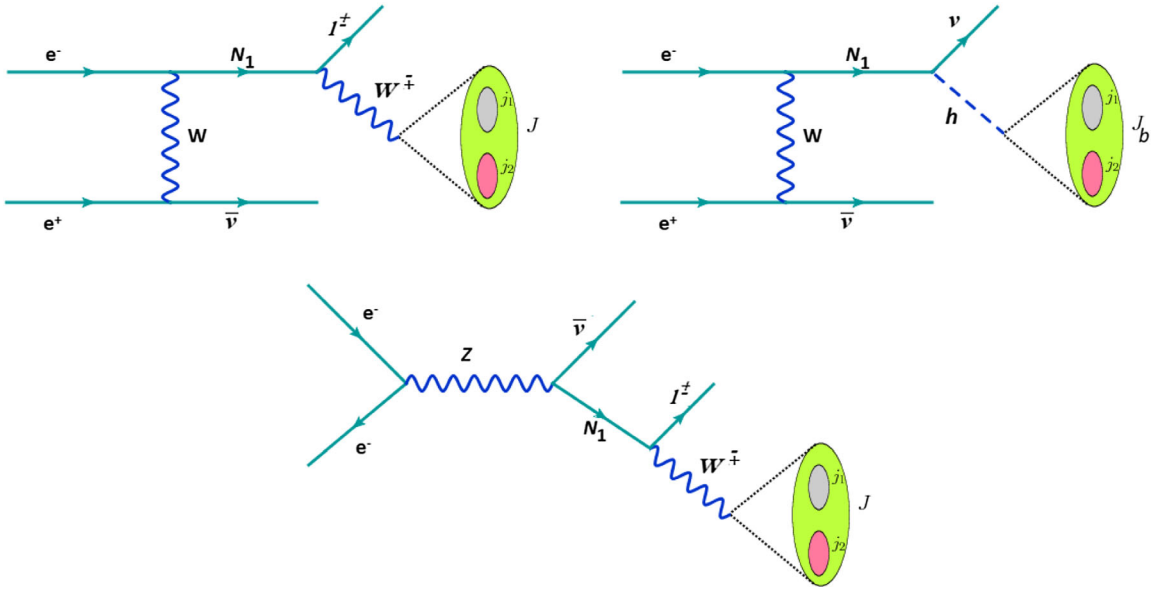

FIG. 8. $e + J + p_T^{\rm miss}$ and $J_b + p_T^{\rm miss}$ final states at the linear colliders.

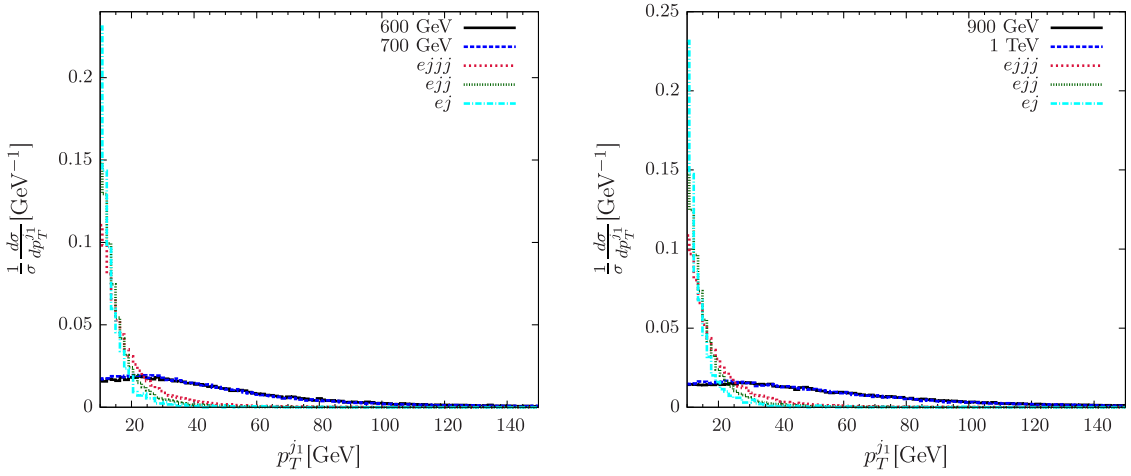

FIG. 9. Transverse momentum distribution of the associated jet ($p_T^{j_1}$) from the signal and background events for $M_N = 600$ GeV and 700 GeV at the $\sqrt{s} = 1.3$ TeV LHeC (left panel) and $M_N = 900$ GeV and 1 TeV at the $\sqrt{s} = 1.8$ TeV LHeC (right panel).

The LNV signal is almost background free until some $e^+ +$ jets events appear from some radiations, however, that effect will be negligible. Therefore for completeness we include the LNC channel where the leading SM backgrounds will come from $e^- jjj$, $e^- jj$, and $e^- j$ including initial state and final state radiations. For completeness we include both of the LNV and LNC channels. Further we use the fat-jet algorithm to reduce the SM backgrounds. We have shown the distributions of the transverse momentum of the leading jet ($p_T^{j_1}$), lepton (p_T^e) and fat jet (p_T^J) in Figs. 9–11. The fat-jet mass distribution (M_J) has been shown in Figs. 12. The invariant mass distribution of the lepton and fat-jet system (M_{eJ}) has been shown in Fig. 13. We have also compared the signals with the corresponding SM backgrounds. As a sample we consider $M_N = 600$ GeV and 700 GeV for $\sqrt{s} =$ 1.3 TeV LHeC and $M_N = 900$ GeV, 1 TeV at $\sqrt{s} =$ 1.8 TeV HE-LHeC as shown in Figs. 9–13.

We have chosen $M_N = 400$ GeV–900 GeV for the 1.3 TeV LHeC and $M_N = 800$ GeV–1.5 TeV for the 1.8 TeV HE-LHeC. As benchmark points we have chosen $M_N = 600$ GeV, 700 GeV at the 1.3 TeV LHeC and $M_N = 900$ GeV, 1.0 TeV at the 1.8 TeV HE-LHeC after the basic cuts. In view of the distributions in Figs. 9–13, we have used the following advanced selection cuts to reduce the backgrounds:

1. *Advanced cuts for $M_N = 400$ GeV – 900 GeV at the $\sqrt{s} = 1.3$ TeV LHeC after the detector simulation*

(i) Transverse momentum for lepton and jet, $p_T^{e^\pm} > 50$ GeV.
(ii) Transverse momentum for fat jet $p_T^J > 175$ GeV.
(iii) Fat-jet mass $M_J > 70$ GeV.
(iv) Invariant mass window of $e^\pm$ and fat-jet J, $|M_{eJ} - M_N| \leq 20$ GeV.

We have noticed that $M_J > 70$ GeV cuts out the low energy peaks ($M_J \leq 25$ GeV) which come from the hadronic activity of the low energy jets. Similarly, the p_T^J and p_T^e cuts are also very effective. Due to the presence of the

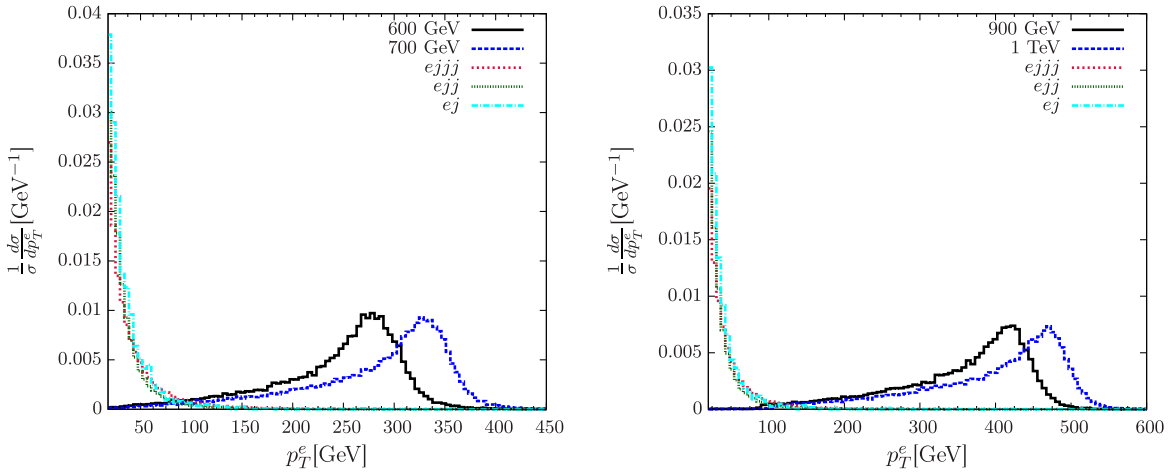

FIG. 10. Transverse momentum distribution of the electron (p_T^e) from the signal and background events for $M_N = 600$ GeV and 700 GeV at the $\sqrt{s} = 1.3$ TeV LHeC (left panel) and $M_N = 900$ GeV and 1 TeV at the $\sqrt{s} = 1.8$ TeV HE-LHeC (right panel).

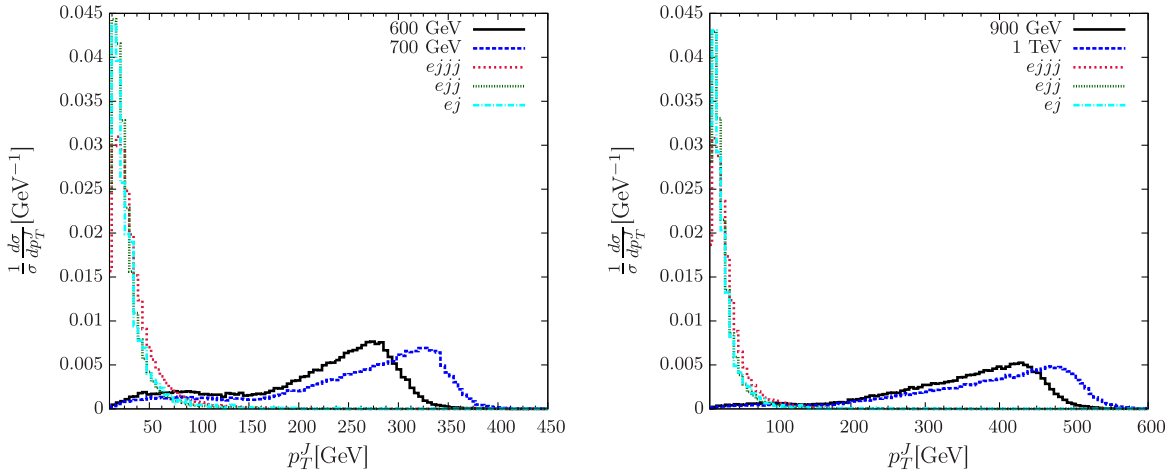

FIG. 11. Transverse momentum distribution of the fat jet (p_T^J) from the signal and background events for $M_N = 600$ GeV and 700 GeV at the $\sqrt{s} = 1.3$ TeV LHeC (left panel) and $M_N = 900$ GeV and 1 TeV at the $\sqrt{s} = 1.8$ TeV HE-LHeC (right panel).

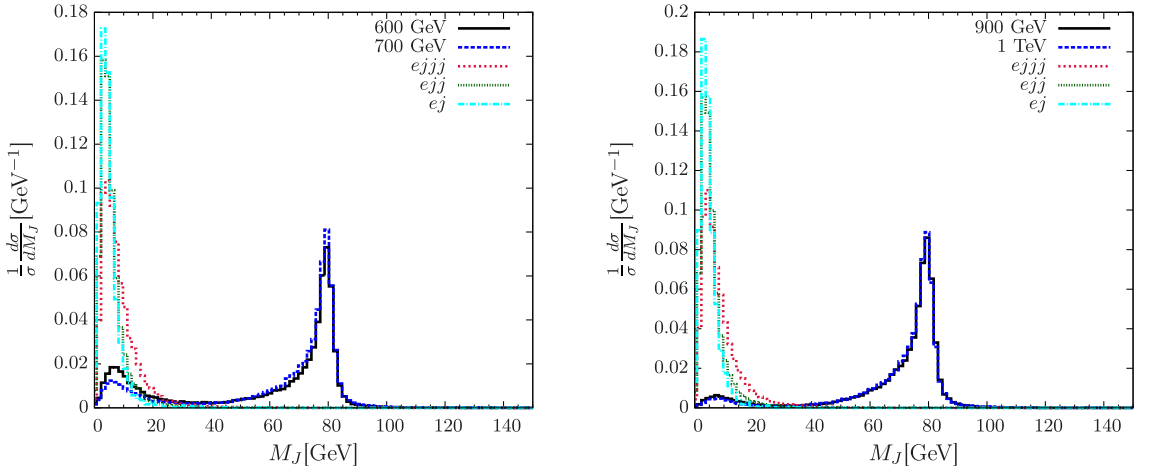

FIG. 12. Jet mass (M_J) distribution of the fat jet from the signal and background events for $M_N = 600$ GeV and 700 GeV at the $\sqrt{s} = 1.3$ TeV LHeC (left panel) and $M_N = 900$ GeV and 1 TeV at the $\sqrt{s} = 1.8$ TeV HE-LHeC (right panel).

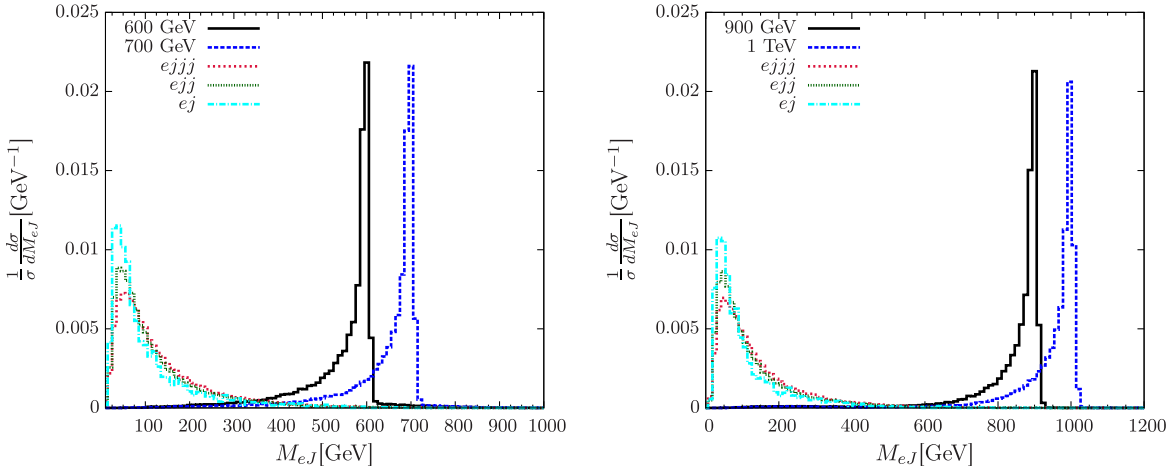

FIG. 13. Invariant mass distribution of the fat jet and electron system (M_{eJ}) from the signal and background events for $M_N = 600$ GeV and 700 GeV at the $\sqrt{s} = 1.3$ TeV LHeC (left panel) and $M_N = 900$ GeV and 1 TeV at the $\sqrt{s} = 1.8$ TeV HE-LHeC (right panel).

RHN, these distributions from the signal will be in the high values than the SM backgrounds. Therefore selecting such cuts at high values, as we have done here, will be extremely useful to reduce the SM backgrounds.

We have noticed that ej background can completely be reduced with the application of the kinematic cuts on p_T^e, p_T^J, and M_J. It is difficult to obtain a fat jet from this process because the t channel exchange of the Z boson and photon will contribute to this process, however, the other low-energy jets may come from the radiations at the initial and final states. These jets do not help to make the fat jets sufficiently energetic. Therefore $p_T^J > 175$ GeV ($p_T^J > 400$ GeV) at the LHeC (HE-LHeC) are very useful. Similarly the $ejjj$ is the irreducible background in this case which will contribute most among the backgrounds. Whereas ejj is the second leading background in this case. However, both of these backgrounds can be reduced using the invariant mass cut of the RHN. As the RHN will decay according to $N \to eJ$, therefore the invariant mass of the eJ system with an window of 20 GeV ($|M_{eJ} - M_N| \leq 20$ GeV) will be extremely useful to reduce the backgrounds further in these colliders. In Table I we have given the two benchmark scenarios at the 1.3 TeV LHeC where the signal events are normalized by the square of the mixing.

2. Advanced cuts for $M_N = 800$ GeV $- 1.5$ TeV at the $\sqrt{s} = 1.8$ TeV HE-LHeC after the detector simulation

(i) Transverse momentum for lepton, $p_T^{e^\pm} > 250$ GeV.
(ii) Transverse momentum for fat jet $p_T^J > 400$ GeV.
(iii) Fat-jet mass $M_J > 70$ GeV.
(iv) Invariant mass window of $e^\pm$ and fat jet J, $|M_{eJ} - M_N| \leq 20$ GeV.

We have chosen $M_N = 900$ GeV and 1 TeV at the $\sqrt{s} = 1.8$ TeV HE-LHeC. The corresponding signals normalized by the square of the mixing and the SM backgrounds are listed in Table II. Due to the heavier mass range of the RHN, we have chosen stronger cuts for the transverse momenta of the electron and fat jet which became useful to reduce the backgrounds.

B. Linear collider analysis for the signal $e^\pm + J + p_T^{\rm miss}$

In the linear collider we study the $e^\pm + J + p_T^{\rm miss}$ signal from the leading decay mode of the RHN at the 1 TeV and 3 TeV center of mass energy. The corresponding distributions for two benchmark points for $M_N = 500$ GeV, 800 GeV at $\sqrt{s} = 1$ TeV and $M_N = 800$ GeV, 2 TeV at $\sqrt{s} = 3$ TeV linear colliders are given in Figs. 14–18 after the basic cuts. We perform a complete cut based analysis for the signal and the SM backgrounds. In this process we have $\nu_e eW$ as the leading background where as WW, ZZ, and $t\bar{t}$ are other important backgrounds.

We have shown the missing momentum ($p_T^{\rm miss}$), transverse momenta of the electron p_T^e and fat jet p_T^J in Figs. 14–16 for the linear colliders. The fat-jet mass M_J distribution has been shown in Fig. 17. We construct the polar angle variable in Fig. 18 for the electron (fat jet), $\cos\theta_e(\cos\theta_J)$ where $\theta_{e(J)} = \tan^{-1}[\frac{p_T^{e(J)}}{p_z^{e(J)}}]$, where $p_z^{e(J)}$ is the z component of the three momentum of the electron (fat jet). This is a very effective cut which reduces the SM background significantly. In view of these distributions, we have used the following advanced selection cuts to reduce the backgrounds:

TABLE I. Cut flow of the signal and background events for the final state $e^\pm + J + j_1$ for $M_N = 600$ GeV and 700 GeV with $\sqrt{s} = 1.3$ TeV LHeC where the signal events are normalized by the square of the mixing.

	Signal		Background		
Cuts	$M_{N_1} = 600$ GeV	$M_{N_1} = 700$ GeV	$ejjj$	ejj	Total
Basic Cuts	645,860	261,254	70,029,800	189,689,000	259,718,800
$p_T^J > 175$ GeV	476,640	214,520	295,658	338,720	634,378
$M_J > 70$ GeV	356,350	160,017	35,244	17,520	52,764
$p_T^e > 50$ GeV	356,126	159,918	33,286	17,520	50,806
$\lvert M_{eJ} - M_N\rvert \leq 20$ GeV	304,457	129,690	7	1	8

TABLE II. Cut flow of the signal and background events for the final state $e^\pm + J + j_1$ for $M_N = 900$ GeV and 1.0 TeV with $\sqrt{s} = 1.8$ TeV HE-LHeC where the signal events are normalized by the square of the mixing.

	Signal		Background		
Cuts	$M_{N_1} = 900$ GeV	$M_{N_1} = 1$ TeV	$ejjj$	ejj	Total
Basic Cuts	427,311	207,015	108,243,000	273,410,000	381,653,000
$p_T^J > 400$ GeV	158,694	110,289	12,225	12,450	24,675
$M_J > 70$ GeV	145,558	96,787	4,596	4,150	8,746
$p_T^e > 250$ GeV	144,997	96,487	4,596	4,150	8,746
$\lvert M_{eJ} - M_N\rvert \leq 20$ GeV	119,659	71,490	3	1	4

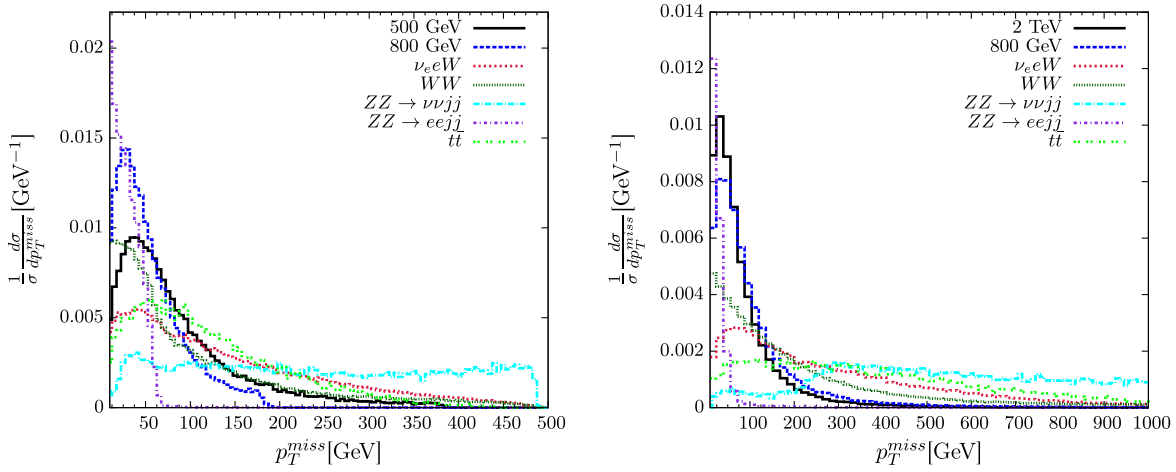

FIG. 14. Missing momentum distribution of the signal and background events for $M_N = 500$ GeV and 800 GeV at the $\sqrt{s} = 1$ TeV (left panel) and $M_N = 800$ GeV and 2 TeV at the $\sqrt{s} = 3$ TeV (right panel) linear colliders.

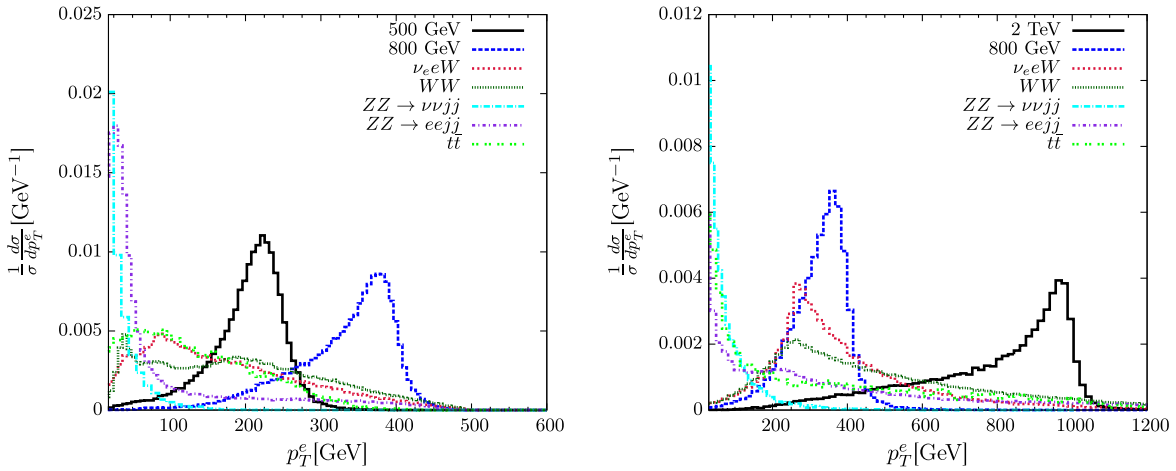

FIG. 15. Transverse momentum distribution of the electron (p_T^e) from the signal and background events for $M_N = 500$ GeV and 800 GeV at the $\sqrt{s} = 1$ TeV (left panel) and $M_N = 800$ GeV and 2 TeV at the $\sqrt{s} = 3$ TeV (right panel) linear colliders.

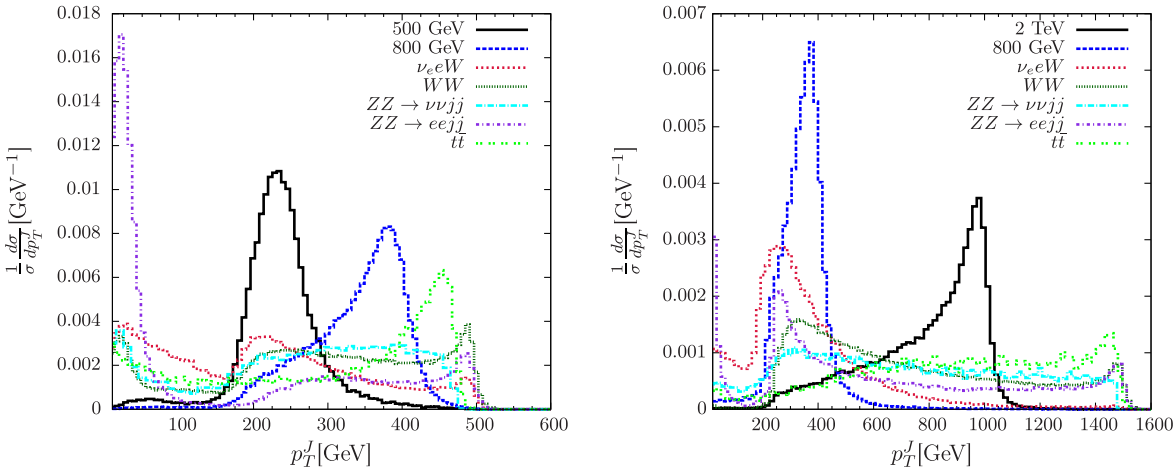

FIG. 16. Transverse momentum distribution of the fat jet (p_T^J) from the signal and background events for $M_N = 500$ GeV and 800 GeV at the $\sqrt{s} = 1$ TeV (left panel) and $M_N = 800$ GeV and 2 TeV at the $\sqrt{s} = 3$ TeV linear colliders.

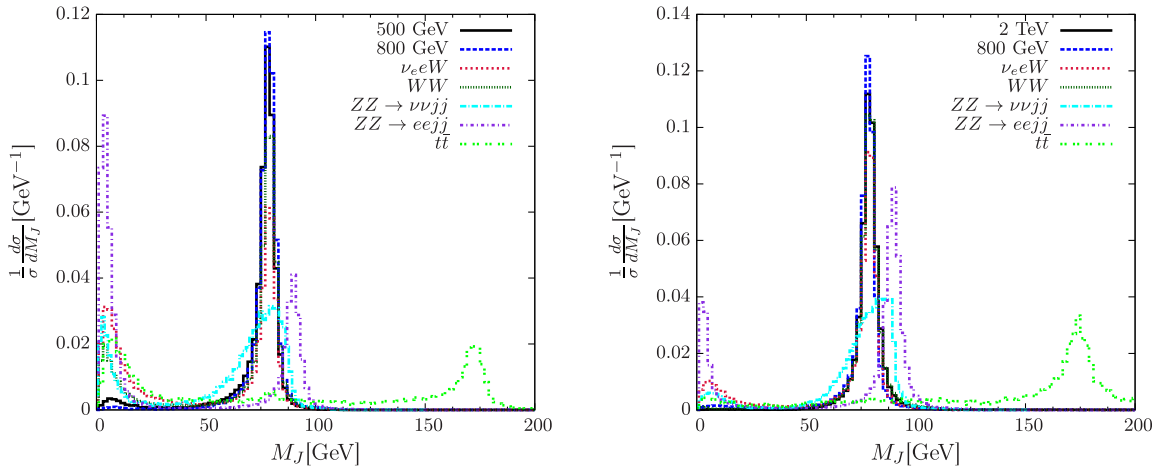

FIG. 17. Jet mass (M_J) distribution of the fat jet from the signal and background events for $M_N = 500$ GeV and 800 GeV at the $\sqrt{s} = 1$ TeV (left panel) and $M_N = 800$ GeV and 2 TeV at the $\sqrt{s} = 3$ TeV (right panel) linear colliders.

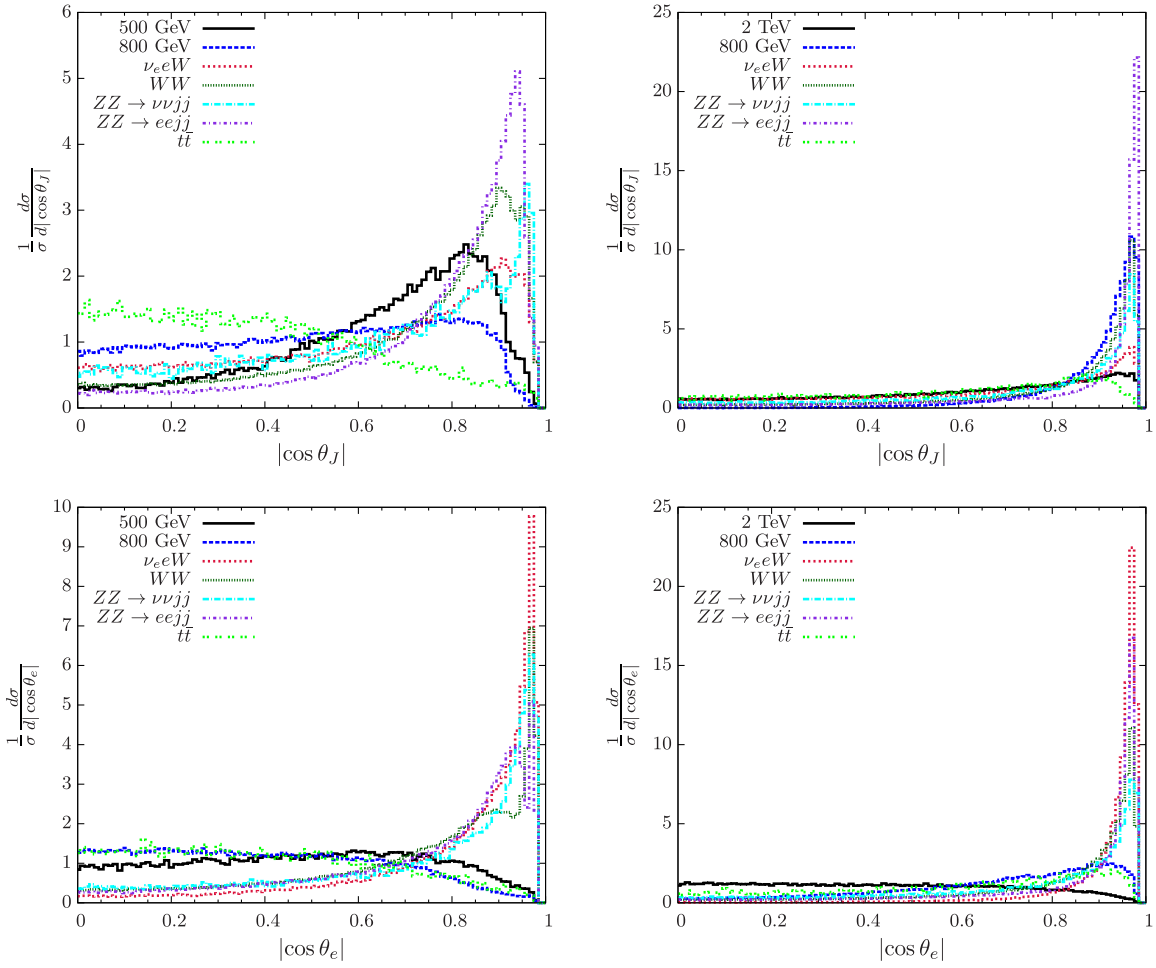

FIG. 18. $\cos\theta_{J(e)}$ distributions for the $J(e)$ in the first row (second row) for the 1 TeV (left column) and 3 TeV (right column) linear colliders.

1. Advanced cuts for $M_N = 400$ GeV – 900 GeV at the $\sqrt{s} = 1$ TeV linear collider after the detector simulation

(i) Transverse momentum for fat jet $p_T^J > 150$ GeV for M_N mass range 400 GeV-600 GeV and $p_T^J > 250$ GeV for M_N mass range 700 GeV-900 GeV.
(ii) Transverse momentum for leading lepton $p_T^{e^\pm} > 100$ GeV for M_N mass range 400 GeV-600 GeV and $p_T^{e^\pm} > 200$ GeV for M_N mass range 700 GeV-900 GeV.
(iii) Polar angle of lepton and fat jet $|\cos\theta_e| < 0.85$, $|\cos\theta_J| < 0.85$.
(iv) Fat-jet mass $M_J > 70$ GeV.

We have tested $M_N = 400$ GeV to 900 GeV at the $\sqrt{s} = 1$ TeV at the linear collider. Hence we consider two benchmark points at the $\sqrt{s} = 1$ TeV linear collider such as $M_N = 500$ GeV and 800 GeV. The cut flow for the $\sqrt{s} = 1$ TeV are given in the Tables III and IV, respectively. We have noticed that $\cos\theta_{e(J)}$ is a very important kinematic variable and setting $|\cos\theta_{e(J)}| < 0.85$ puts a very strong cut for the SM backgrounds. The $M_J > 70$ GeV is also effective to cut out the low mass peaks (1 GeV $\leq M_J \leq 25$ GeV) from the low energy jets.

2. Advanced cuts for $M_N = 700$ GeV – 2.9 TeV at the $\sqrt{s} = 3$ TeV linear collider after the detector simulation

(i) Transverse momentum for fat jet $p_T^J > 250$ GeV for the M_N mass range 700 GeV-900 GeV and $p_T^J > 400$ GeV for M_N mass range 1–2.9 TeV.

TABLE III. Cut flow for the signal and background events for the final state $e^\pm + J + p_T^{\rm miss}$ for $M_N = 500$ GeV at the $\sqrt{s} = 1$ TeV linear collider. The signal events are normalized by the square of the mixing.

		Background				
Cuts	Signal	$\nu_e eW$	WW	ZZ	$t\bar{t}$	Total
Basic Cuts	12,996,200	201,586	72,244	7,200	4,300	285,330
$\lvert\cos\theta_J\rvert \leq 0.85$	12,789,800	148,802	44,910	3,800	4,100	201,600
$\lvert\cos\theta_e\rvert \leq 0.85$	12,671,800	79,008	40,574	2,800	3,900	126,280
$p_T^J > 150$ GeV	12,308,300	70,669	40,490	2,300	3,200	116,660
$M_J > 70$ GeV	10,923,100	62,303	37,043	2,100	2,300	103,700
$p_T^{\ell} > 100$ GeV	10,714,500	57,076	33,488	1,400	1,530	93,400

TABLE IV. Cut flow for the signal and background events for the final state $e^\pm + J + p_T^{\rm miss}$ for $M_N = 800$ GeV at the $\sqrt{s} = 1$ TeV linear collider. The signal events are normalized by the square of the mixing.

		Background				
Cuts	Signal	$\nu_e eW$	WW	ZZ	$t\bar{t}$	Total
Basic Cuts	8,684,990	201,586	72,244	7,200	4,300	285,330
$\lvert\cos\theta_J\rvert \leq 0.85$	8,649,570	148,802	44,910	3,800	4,100	201,600
$\lvert\cos\theta_e\rvert \leq 0.85$	8,618,420	79,008	40,574	2,800	3,900	126,280
$p_T^J > 250$ GeV	7,681,440	59,001	40,329	2,303	2,720	104,354
$M_J > 70$ GeV	7,176,280	53,990	36,997	2,187	2,282	95,437
$p_T^{\ell} > 200$ GeV	7,080,200	38,729	26,208	942	613	66,493

TABLE V. Cut flow for the signal and background events for the final state $e^\pm + J + p_T^{\rm miss}$ for $M_N = 800$ GeV at the $\sqrt{s} = 3$ TeV linear collider. The signal events are normalized by the square of the mixing.

		Background				
Cuts	Signal	$\nu_e eW$	WW	ZZ	$t\bar{t}$	Total
Basic Cuts	21,789,900	193,533	12,135	1,361	271	207,301
$\lvert\cos\theta_J\rvert \leq 0.85$	13,599,300	126,980	4,766	406	215	132,367
$\lvert\cos\theta_e\rvert \leq 0.85$	12,163,300	21,110	4,609	390	195	26,304
$p_T^J > 250$ GeV	12,083,500	18,619	4,607	390	189	23,807
$M_J > 70$ GeV	11,287,000	17,442	4,411	385	176	22,416
$p_T^{\ell} > 200$ GeV	11,094,300	16,915	4,108	343	104	21,470

TABLE VI. Cut flow for the signal and background events for the final state $e^{\pm} + J + p_T^{\rm miss}$ for $M_N = 2$ TeV at the $\sqrt{s} = 3$ TeV linear collider. The signal events are normalized by the square of the mixing.

		Background				
Cuts	Signal	$\nu_e eW$	WW	ZZ	$t\bar{t}$	Total
Basic Cuts	13,822,500	193,533	12,135	1,382	271	207,322
$\lvert\cos\theta_J\rvert \leq 0.85$	12,701,600	126,980	4,766	412	215	132,374
$\lvert\cos\theta_e\rvert \leq 0.85$	12,647,200	21,110	4,609	396	195	26,310
$p_T^J > 400$ GeV	12,611,000	15,737	4,605	396	184	20,923
$M_J > 70$ GeV	12,015,600	14,889	4,410	391	175	19,865
$p_T^{e} > 250$ GeV	11,987,000	14,184	4,010	336	10	18,630

(ii) Transverse momentum for leading lepton $p_T^{e^{\pm}} > 200$ GeV for M_N mass range 700 GeV–900 GeV and $p_T^{e^{\pm}} > 250$ GeV for M_N mass range 1–29 TeV.
(iii) Polar angle of lepton and fat jet $\lvert\cos\theta_e\rvert < 0.85$, $\lvert\cos\theta_J\rvert < 0.85$.
(iv) Fat-jet mass $M_J > 70$ GeV.

We have tested $M_N = 700$ GeV to 2.9 TeV at the $\sqrt{s} = 3$ TeV at the linear collider. Hence we consider two benchmark points at the $\sqrt{s} = 3$ TeV linear collider such as $M_N = 800$ GeV and 2 TeV. The cut flow for the benchmark points at the $\sqrt{s} = 3$ TeV are given in the Tables V and VI respectively. At the 3 TeV we see almost the same behavior for the kinematic variables as we noticed at the 1 TeV case except the p_T distributions of the electron and fat jet. At this point we must mention that the backgrounds like ZZ and $t\bar{t}$ can have more than one lepton in the final state which has been efficiently vetoed to reduce the effect.

C. Linear collider analysis for the signal $J_b + p_T^{\rm miss}$

Considering the $N \to h\nu$, $h \to J_b$ mode at the linear collider we obtain the $J_b + p_T^{\rm miss}$ final state. For this final state the dominant SM backgrounds come from the processes $h\nu_\ell\bar{\nu}_\ell$ and $Z\nu_\ell\bar{\nu}_\ell$. Backgrounds can also come from the intermediate processes ZZ and ZH. We have generated the background events combining all these processes in MadGraph for our analysis.

In Figs. 19, 20, and 21, we plot the missing momentum $(p_T^{\rm miss})$, transverse momentum of the fat-b jet $p_T^{J_b}$ and jet mass of the fat-b jet (M_{J_b}) distributions for $M_N = 700$ GeV and 800 GeV at the $\sqrt{s} = 1$ TeV linear collider and $M_N = 1.5$ TeV and 2 TeV at the $\sqrt{s} = 3$ TeV linear collider. In view of these distributions, we have used the following advanced selection cuts to reduce the SM background:

1. Advanced cuts for $M_N = 400$ GeV – 900 GeV at the $\sqrt{s} = 1$ TeV linear collider after the detector simulation

(i) Transverse momentum for J_b, $p_T^{J_b} > 250$ GeV.
(ii) Fat-b mass, $M_{J_b} > 115$ GeV.
(iii) Missing energy, $p_T^{\rm miss} > 150$ GeV.

We consider two benchmark points such as $M_N = 700$ GeV and 800 GeV at the 1 TeV linear collider to produce the boosted Higgs from RHNs. The cut flow has been shown in Tab. VII. The b-jets are coming from the SM h as the M_{J_b} distribution peaks at the Higgs mass for the signal at the linear colliders. As a result $M_{J_b} > 115$ GeV sets a strong cut on the SM backgrounds.

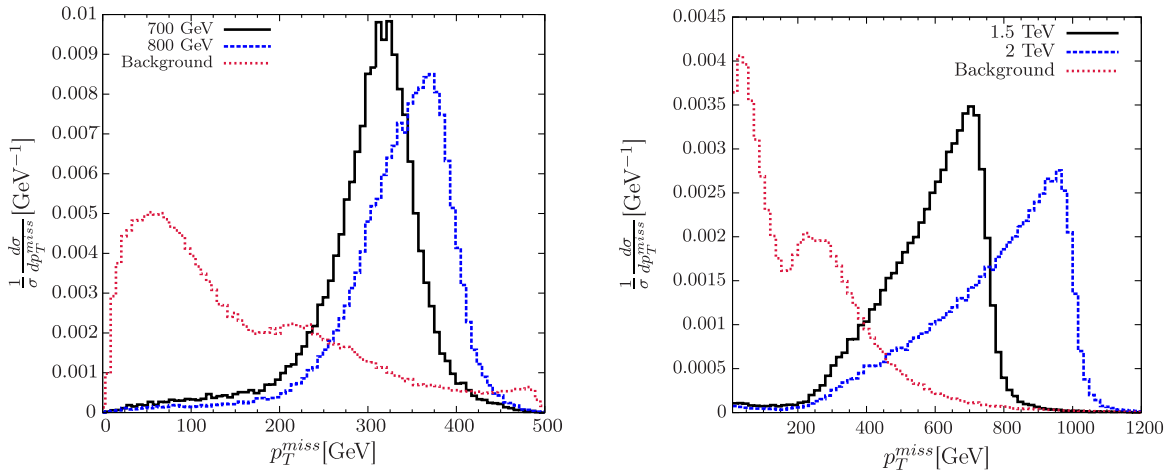

FIG. 19. $p_T^{\rm miss}$ distribution of the signal and background events for $M_N = 700$ GeV and 800 GeV at the $\sqrt{s} = 1$ TeV (left panel) and $M_N = 1.5$ TeV and 2 TeV at the $\sqrt{s} = 3$ TeV (right panel) linear colliders.

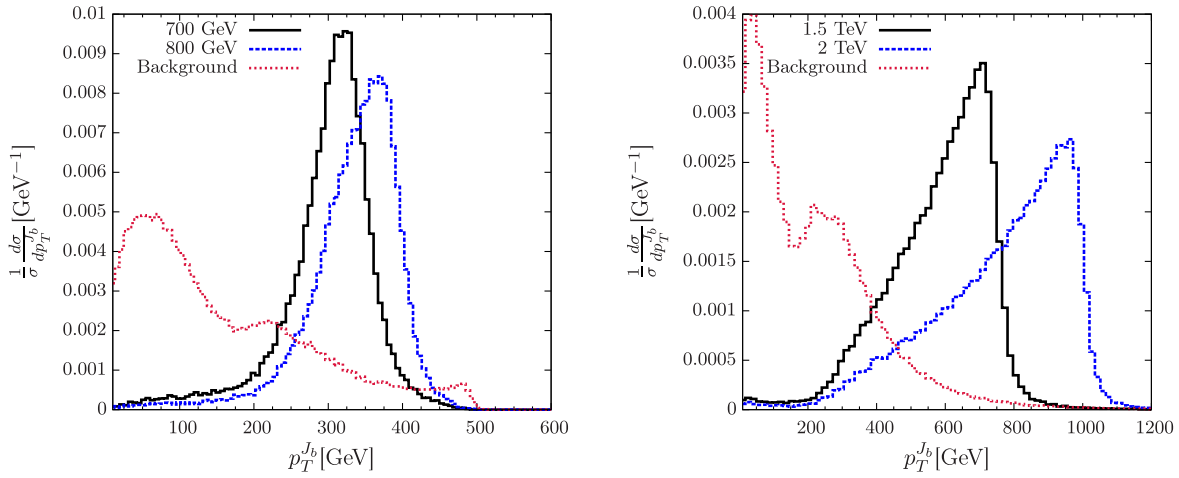

FIG. 20. Transverse momentum distribution of J_b ($p_T^{J_b}$) from the signal and background events for $M_N = 700$ GeV and 800 GeV at the $\sqrt{s} = 1$ TeV (left panel) and $M_N = 1.5$ TeV and 2 TeV at the $\sqrt{s} = 3$ TeV (right panel) linear colliders.

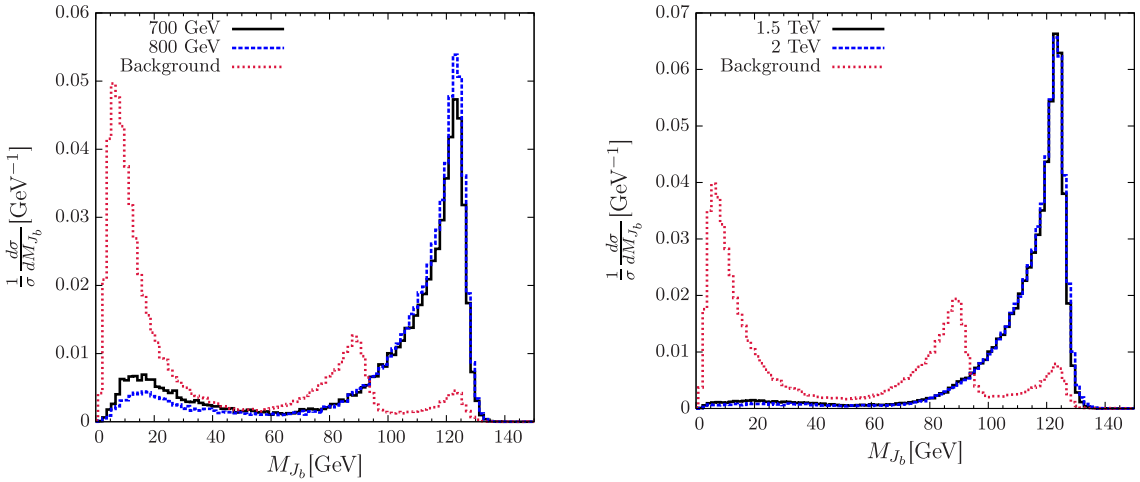

FIG. 21. Fat b-Jet mass (M_{J_b}) distribution from the signal and background events for $M_N = 700$ GeV and 800 GeV at the $\sqrt{s} = 1$ TeV (left panel) and $M_N = 1.5$ TeV and 2 TeV at the $\sqrt{s} = 3$ TeV (right panel) linear colliders.

2. Advanced cuts for the $M_N = 1$ TeV − 2.9 TeV for the $\sqrt{s} = 3$ TeV linear collider after the detector simulation

(i) Transverse momentum for fat-b (J_b), $p_T^{J_b} > 350$ GeV.
(ii) Fat-b mass, $M_{J_b} > 115$ GeV.
(iii) Missing energy, $p_T^{\text{miss}} > 175$ GeV.

We consider two benchmark points such as $M_N = 1.5$ TeV and 2 TeV at the 3 TeV linear collider for the boosted Higgs production from the RHN. The cut flow has been shown in Table VIII. The b-jets are coming from the

TABLE VII. Cut flow for the signal and background events for the final state $J_b + p_T^{\text{miss}}$ for $M_N = 700$ GeV and 800 GeV at the $\sqrt{s} = 1$ TeV linear collider. The signal events are normalized by the square of the mixing.

	Signal		
Cuts	$M_N = 700$ GeV	$M_N = 800$ GeV	Background
Basic Cuts	1,288,150	1,248,340	19,300
$p_T^{\text{miss}} > 150$ GeV	1,239,440	1,223,480	8,373
$p_T^{J_b} > 250$ GeV	1,100,790	1,153,650	4,239
$M_{J_b} > 115$ GeV	609,330	661,258	855

TABLE VIII. Cut flow for the signal and background events for the final state $J_b + p_T^{\text{miss}}$ for $M_N = 1.5$ TeV and 2 TeV at the $\sqrt{s} = 3$ TeV linear collider. The signal events are normalized by the square of the mixing.

	Signal		
Cuts	$M_N = 1.5$ TeV	$M_N = 2$ TeV	Background
Basic Cuts	5,077,160	4,043,130	74,245
$p_T^{\text{miss}} > 175$ GeV	5,005,240	4,011,420	39,231
$p_T^{J_b} > 350$ GeV	4,731,550	3,902,490	15,327
$M_{J_b} > 115$ GeV	2,961,620	2,479,960	3,740

SM h as the M_{J_b} distribution peaks at the Higgs mass for the signal at the linear colliders. As a result $M_{J_b} > 115$ GeV sets a strong cut on the SM backgrounds. We also consider a strong $p_T^{J_b} > 350$ GeV cut for the high mass RHNs at the 3 TeV collider. In this work, we adopt a minimalistic approach and consider a flat 70% tagging efficiency for each of the daughter b jets coming from the Higgs decay.

IV. CURRENT BOUNDS

The bounds on the light-heavy neutrino mixing for the electron flavor comes from a variety of searches. As we are interested on the RHN of mass $M_N \geq 100$ GeV, therefore we will compare our results with such bounds which are important for that mass range. The electroweak precision data (EWPD) bounds have been calculated in [105–107] which obtains the bound on $|V_{eN}|^2$ as 1.681×10^{-3} at the 95% C. L., the LEP2 [108], calculated at the 95% C.L., bounds are rather weaker except $M_N = 108$ GeV where it touches the EWPD line. The strongest bounds are coming from the GERDA [109] $0\nu2\beta$ study where the limits as calculated in [13] up to $M_N = 959$ GeV. The lepton universality limits from [110] set bounds on $|V_{eN}|^2$ at 6.232×10^{-4} up to $M_N = 1$ TeV at the 95% C. L. These bounds are plotted in Figs. 22–27.

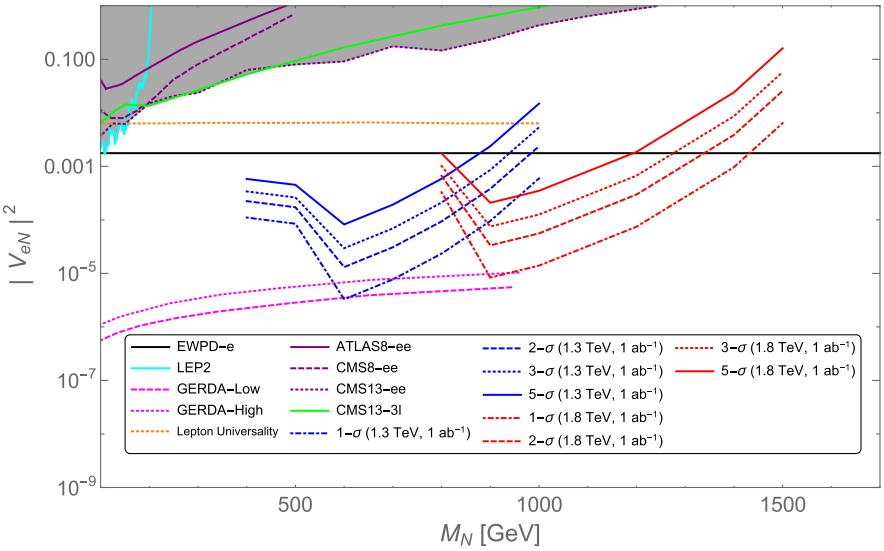

FIG. 22. The prospective upper limits on $|V_{eN}|^2$ at the 1.3 TeV LHeC (blue band) and 1.8 TeV HE-LHeC (red band) at the 1 ab^{-1} luminosity compared to EWPD [105–107], LEP2 [108], GERDA [109] $0\nu2\beta$ study from [13], ATLAS (ATLAS8-ee) [111], CMS (CMS8-ee) [112] at the 8 TeV LHC, 13 TeV CMS search for $e^{\pm}e^{\pm} + 2j$ (CMS13-ee) [113] and 13 TeV CMS search for 3ℓ (CMS13-ee) [113], respectively.

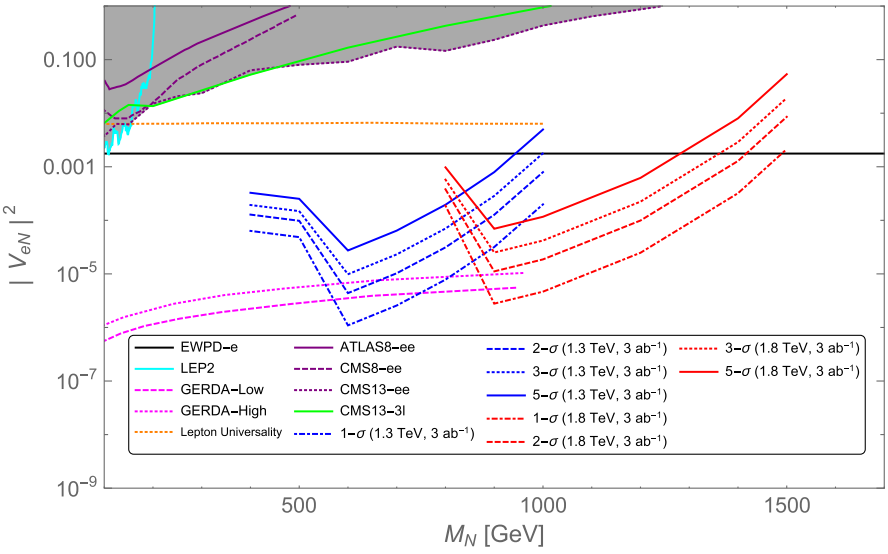

FIG. 23. Same as Fig. 22 with 3 ab^{-1} luminosity at the 1.3 TeV LHeC and 1.8 TeV HE-LHeC.

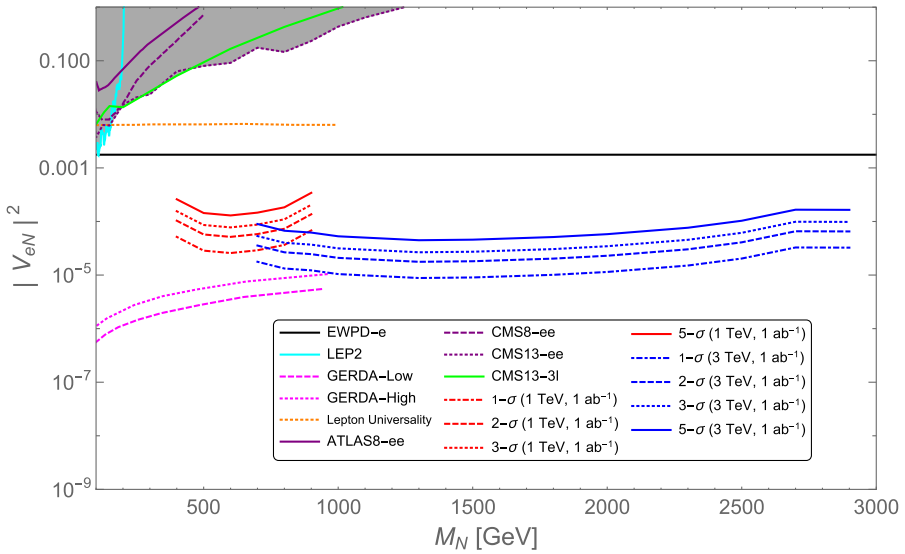

FIG. 24. The prospective upper limits on $|V_{eN}|^2$ at the 1 TeV (red band) and 3 TeV (blue band) linear colliders at the 1 ab^{-1} luminosity for $e + J + p_T^{\rm miss}$ signal compared to EWPD [105–107], LEP2 [108], GERDA [109] $0\nu2\beta$ study from [13], ATLAS (ATLAS8-ee) [111], CMS (CMS8-ee) [112] at the 8 TeV LHC, 13 TeV CMS search for $e^{\pm}e^{\pm} + 2j$ (CMS13-ee) [113] and 13 TeV CMS search for 3ℓ (CMS13-ee) [113], respectively.

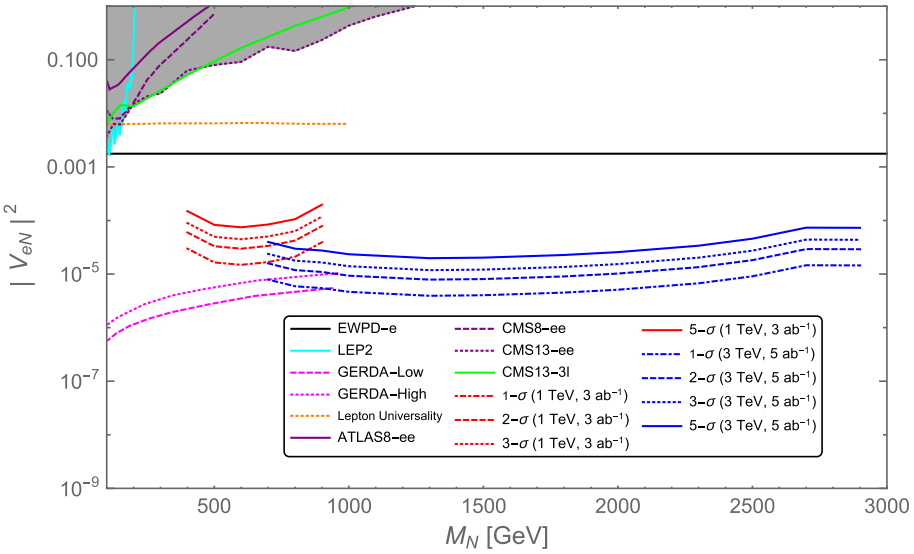

FIG. 25. Same as Fig. 24 with 3(5) ab^{-1} luminosity at the 1(3) TeV linear collider.

Apart from the above mentioned indirect searches, the recent collider searches for the LHC also set bounds $|V_{eN}|^2$ at the $\sqrt{s} = 8$ TeV at 95% C. L. from same sign dilepton plus dijet search. The bounds on $|V_{eN}|^2$ from ATLAS (ATLAS8-ee) [111] and CMS (CMS8-ee) [112] are obtained at 23.3 fb^{-1} and 19.7 fb^{-1} luminosities respectively for the $e^{\pm}e^{\pm} + 2j$ sample. The ATLAS limit is weaker than the CMS limits for 100 GeV $\leq M_N \leq$ 500 GeV. The LHC has also published the recent results at $\sqrt{s} = 13$ TeV with 35.9 fb^{-1} luminosity which set stronger bounds on $|V_{eN}|^2$ than the previous direct searches for 100 GeV $\leq M_N \leq$ 500 GeV. The bounds on $|V_{eN}|^2$ from the $e^{\pm}e^{\pm} + 2j$ signal in CMS (CMS13-ee) [113] and from trilepton search at CMS (CMS13 $- 3\ell$) [114] are also competitive, however, weaker than the EWPD for 100 GeV $\leq M_N \leq$ 1.2 TeV. These limits are also plotted in Figs. 22–27.

We have explored that at the LHeC with $\sqrt{s} = 1.3$ TeV collider energy and 1 ab^{-1} luminosity, the bound on $|V_{eN}|^2$ for $MN_N = 600$ GeV with $1 - \sigma$ C.L. is better than the $0\nu2\beta$ limit from GERDA-low where as $M_N \geq 959$ GeV at $1 - \sigma$ limit can be probed better than the GERDA-low and high limit [13,109]. The GERDA limits are stronger for the M_N benchmarks we have studied. The results have been

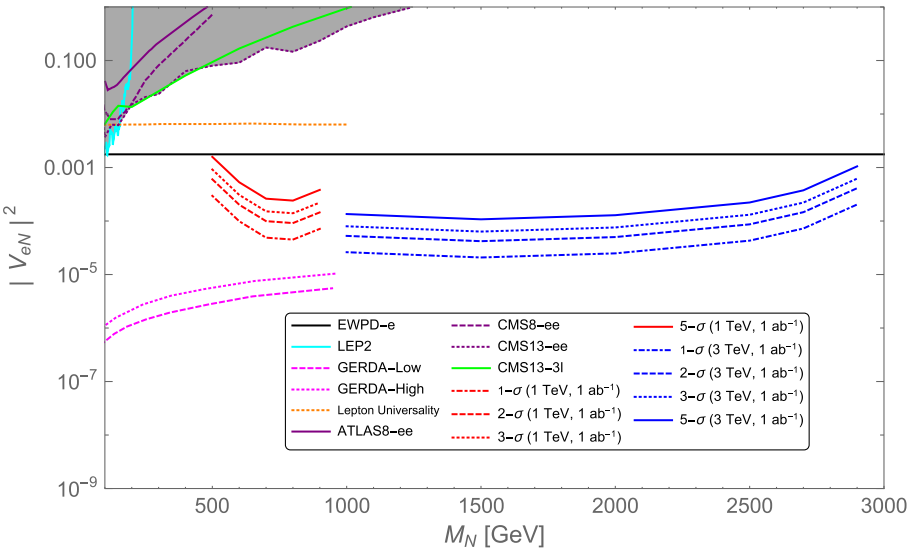

FIG. 26. The prospective upper limits on $|V_{eN}|^2$ at the 1 TeV (red band) and 3 TeV (blue band) linear colliders at the 1 ab^{-1} luminosity for $J_b + p_T^{\rm miss}$ signal compared to EWPD [105–107], LEP2 [108], GERDA [109] $0\nu2\beta$ study from [13], ATLAS (ATLAS8-ee) [111], CMS (CMS8-ee) [112] at the 8 TeV LHC, 13 TeV CMS search for $e^{\pm}e^{\pm} + 2j$ (CMS13-ee) [113] and 13 TeV CMS search for 3ℓ (CMS13-ee) [113], respectively.

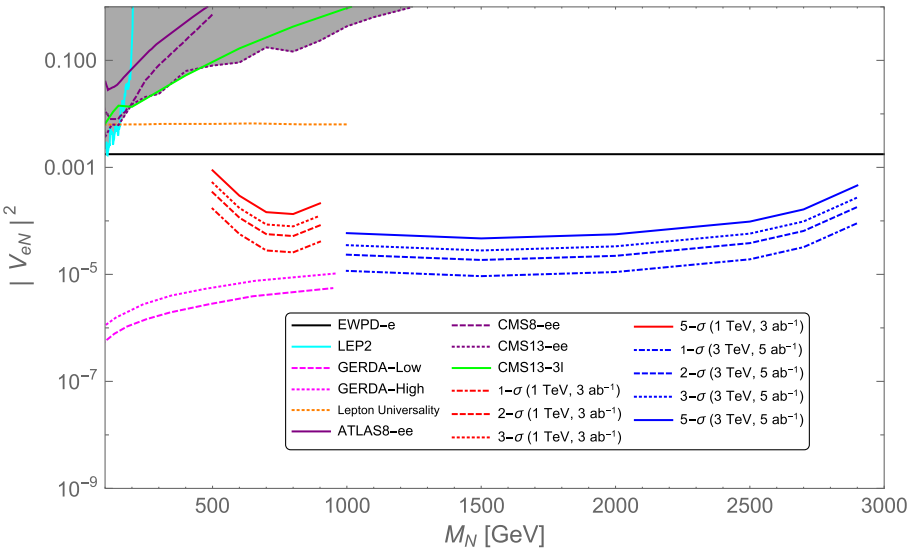

FIG. 27. Same as Fig. 26 with 3(5) ab^{-1} luminosity at the 1(3) TeV linear collider.

shown in Fig. 22. In the same figure we show the bounds obtained from the HE-LHeC with $\sqrt{s} = 1.8$ TeV collider energy and 1 ab^{-1} luminosity. In this case the current GERDA bounds are stronger up to $M_N = 959$ GeV [13,109]. At the HE-LHeC RHN up to $M_N = 1.2$ TeV can be probed at $5-\sigma$ and these bounds could be stronger than the limits obtained from the EWPD-e limit [105–107]. The improved scenario at the 3 ab^{-1} luminosity for the LHeC and HE-LHeC are shown in Figs. 23.

At the linear collider we have explored two sets of signals. one is the $e + J + p_T^{\rm miss}$ and the other one is $J_b + p_T^{\rm miss}$. Using $e + J + p_T^{\rm miss}$ signal at the 1 TeV linear collider we have probed RHNs between 400 GeV $\leq M_N \leq$ 900 GeV at $5-\sigma$ but the $0\nu2\beta$ limit from GERDA [13] is stronger than this result for $M_N \leq 959$ GeV, however, the bounds on $|V_{eN}|^2$ for the RHNs heavier than 1 TeV can be probed at $5-\sigma$ significance or more at the linear collider with the 3 TeV center of mass energy. All the results are. In this case apart from the fat jet properties, the polar angle cut for the leptons worked nicely. The results are shown in Fig. 24. We have also studied the linear colliders at 1 (3) TeV center of mass energy with 3(5) ab^{-1} luminosity. We can find the improved results in Fig. 25. Using the $J_b + p_T^{\rm miss}$ signal we did a complementarity check where

$M_N \geq 1$ TeV can be probed better than GERDA [13] at $5-\sigma$ significance or more at the 3 TeV linear collider. The linear collider can probe $|V_{eN}|^2$ down to $\mathcal{O}(10^{-5})$ for $M_N = 1.35$ TeV at 3 TeV, however, compared to this the bounds obtained at the 1 TeV linear collider are weaker. The corresponding bounds at the $\sqrt{s} = 1$ TeV and 3 TeV linear collider are plotted in Figs. 24 and 26. The red (blue) band represents the bounds on $|V_{eN}|^2$ at 1 TeV (3 TeV) linear collider at different confidence levels. Comparing the bounds between the final states $e + J + p_T^{\rm miss}$ and $J_b + p_T^{\rm miss}$ we find that the former one puts slightly stronger limits on $|V_{eN}|^2$. The results are shown in Fig. 26. We have also studied the linear colliders at 1(3) TeV center of mass energy with 3(5) ab^{-1} luminosity. We can find the improved results in Fig. 27. Finally we comment that our results at the linear collider are stronger than the limits obtained from the EWPD-e [105–107] throughout the study.

V. CONCLUSION

We have studied the RHNs which can be responsible for the generation of the tiny light neutrino masses. We have calculated the production cross sections for the RHNs at the LHeC and linear collider at various center of mass energies and followed by that we have tested the discovery prospects of this RHNs. We have chosen $\sqrt{s} = 1.3$ TeV and 1.8 TeV for the LHeC and $\sqrt{s} = 1$ TeV and 3 TeV for the linear collider. We have considered the sufficiently heavy mass range of the RHNs. These RHNs can decay dominantly into ℓW mode. A massive RHN can sufficiently boost the W such that its hadronic decay modes can form a fat jet. Therefore we study $e + j_1 + J$ and $e + J + p_T^{\rm miss}$ at the LHeC and linear collider respectively. Similarly we consider another interesting mode $N \to h\nu$, $h \to b\bar{b}$ where a boosted SM Higgs can produce a fat b-jet and test the $J_b + p_T^{\rm miss}$ final state at the linear collider. Simulating the events and passing through the selection cuts for the different colliders we calculate the bounds on $|V_{eN}|^2$ at different luminosities and compare with the existing bounds. Hence we conclude that $M_N \geq 959$ GeV can be successfully probed at the 1.8 TeV at the at $5-\sigma$ C. L. with 1 ab^{-1} and 3 ab^{-1} luminosities, respectively. Whereas $M_N \leq 2.9$ TeV can be probed at the 3 TeV linear collider with more than $5-\sigma$ C.L using the $e + J + p_T^{\rm miss}$ signal. A complementary signal of $J_b + p_T^{\rm miss}$ can be useful, too but this is weaker than the bounds obtained by the $e + J + p_T^{\rm miss}$ final state.

ACKNOWLEDGMENTS

The work of S.N. and S.J. was in part supported by U.S. Department of Energy Grant No. DE-SC 0016013. A.D. would like to thank Oliver Fischer for useful discussions on the LHeC and sharing the DELPHES card for that detector. A. D. would also like to thank Daniel Jeans (KEK), Kentarou Mawatari (Osaka University) and Junping Tian (KEK) for useful information regarding the linear collider card in DELPHES.

Note added.—While in final drafting phase, we noticed Ref. [115] appeared in arXiv which also studied fat jet signatures from RHNs at the linear colliders. We have studied LHeC and linear collider at different center of mass energies using detailed cut based analyses. We have compared our results with all the existing bounds using the decay modes of the RHNs to W and SM h bosons. The $0\nu2\beta$ bound became very strong up to $M_N = 959$ GeV. At the linear collider the polar angle variable for the lepton became very useful for us. In our analysis we have showed that high mass RHNs can be observed at $5-\sigma$ significance or more in these colliders.

[1] S. Weinberg, Baryon and Lepton Nonconserving Processes, Phys. Rev. Lett. **43**, 1566 (1979).

[2] P. Minkowski, $\mu \to e\gamma$ at a rate of one out of 10^9 muon decays, Phys. Lett. **67B**, 421 (1977); M. Gell-Mann, P. Ramond, and R. Slansky, in *Supergravity*, edited by P. van Nieuwenhuizen and D. Z. Freedman (North-Holland, Amsterdam, 1979); Conf. Proc. C **790927**, 315 (1979); T. Yanagida, Horizontal symmetry and masses of neutrinos, Conf. Proc. C **7902131**, 95 (1979); T. Yanagida, in *Proceedings of the Workshop on the Unified Theory and the Baryon number in the Universe*, edited by O. Sawada and A. Sugamoto, KEK Report No. 79-18, Tsukuba, Japan, 1979; R. N. Mohapatra and G. Senjanovic, Phys. Rev. Lett. **44**, 912 (1980); J. Schechter and J. W. F. Valle, Neutrino masses in SU(2) × U(1) theories, Phys. Rev. D **22**, 2227 (1980).

[3] M. Magg and C. Wetterich, Phys. Lett. **94B**, 61 (1980); R. N. Mohapatra and G. Senjanovic, Neutrino Mass and Spontaneous Parity Violation, Phys. Rev. Lett. **44**, 912 (1980); R. N. Mohapatra and G. Senjanovic, Phys. Rev. D **23**, 165 (1981); G. Lazarides, Q. Shafi, and C. Wetterich, Proton lifetime and fermion masses in an SO(10) model, Nucl. Phys. **B181**, 287 (1981); E. Ma and U. Sarkar, Phys. Rev. Lett. **80**, 5716 (1998).

[4] R. Foot, H. Lew, X. G. He, and G. C. Joshi, Z. Phys. C **44**, 441 (1989); E. Ma, Pathways to Naturally Small Neutrino Masses, Phys. Rev. Lett. **81**, 1171 (1998).

[5] R. N. Mohapatra, Mechanism for Understanding Small Neutrino Mass in Superstring Theories, Phys. Rev. Lett. **56**, 561 (1986); R. N. Mohapatra and J. W. F. Valle, Neutrino mass and baryon number nonconservation in superstring models, Phys. Rev. D **34**, 1642 (1986).

[6] A. Zee, A theory of lepton number violation, neutrino majorana mass, and oscillation, Phys. Lett. **93B**, 389 (1980); Phys. Lett. **95B**, 461 (1980); T. P. Cheng and L. F. Li, Phys. Rev. D **22**, 2860 (1980); D. Chang and R. N. Mohapatra, Small and Calculable Dirac Neutrino Mass, Phys. Rev. Lett. **58**, 1600 (1987); K. S. Babu, Model of "calculable" Majorana neutrino masses, Phys. Lett. B **203**, 132 (1988); T. Appelquist and R. Shrock, Neutrino masses in theories with dynamical electroweak symmetry breaking, Phys. Lett. B **548**, 204 (2002).

[7] Q. R. Ahmad *et al.* (SNO Collaboration), Direct Evidence for Neutrino Flavor Transformation from Neutral Current Interactions in the Sudbury Neutrino Observatory, Phys. Rev. Lett. **89**, 011301 (2002); Q. R. Ahmad *et al.* (SNO Collaboration), Measurement of Day and Night Neutrino Energy Spectra at SNO and Constraints on Neutrino Mixing Parameters, Phys. Rev. Lett. **89**, 011302 (2002); J. Hosaka *et al.* (Super-Kamiokande Collaboration), Three flavor neutrino oscillation analysis of atmospheric neutrinos in Super-Kamiokande, Phys. Rev. D **74**, 032002 (2006); K. Eguchi *et al.* (KamLAND Collaboration), First Results from KamLAND: Evidence for Reactor Anti-Neutrino Disappearance, Phys. Rev. Lett. **90**, 021802 (2003); M. H. Ahn *et al.* (K2K Collaboration), Indications of Neutrino Oscillation in a 250 km Long Baseline Experiment, Phys. Rev. Lett. **90**, 041801 (2003); K. Abe *et al.* (T2K Collaboration), Indication of Electron Neutrino Appearance from an Accelerator-Produced Off-Axis Muon Neutrino Beam, Phys. Rev. Lett. **107**, 041801 (2011).

[8] K. N. Abazajian *et al.*, Light sterile neutrinos: A white paper, arXiv:1204.5379.

[9] E. Bertuzzo, S. Jana, P. A. N. Machado, and R. Zukanovich Funchal, A dark neutrino portal to explain MiniBooNE, arXiv:1807.09877; E. Bertuzzo, S. Jana, P. A. N. Machado, and R. Zukanovich Funchal, Neutrino masses and mixings dynamically generated by a light dark sector, Phys. Lett. B **791**, 210 (2019).

[10] F. del Aguila and J. A. Aguilar-Saavedra, Distinguishing seesaw models at LHC with multi-lepton signals, Nucl. Phys. **B813**, 22 (2009).

[11] A. Atre, T. Han, S. Pascoli, and B. Zhang, The search for heavy Majorana neutrinos, J. High Energy Phys. 05 (2009) 030.

[12] A. Datta, M. Guchait, and A. Pilaftsis, Probing lepton number violation via majorana neutrinos at hadron supercolliders, Phys. Rev. D **50**, 3195 (1994).

[13] F. F. Deppisch, P. S. Bhupal Dev, and A. Pilaftsis, Neutrinos and collider physics, New J. Phys. **17**, 075019 (2015).

[14] A. Bhardwaj, A. Das, P. Konar, and A. Thalapillil, Looking for minimal inverse seesaw scenarios at the LHC with jet substructure techniques, arXiv:1801.00797.

[15] A. Das, P. Konar, and A. Thalapillil, Jet substructure shedding light on heavy Majorana neutrinos at the LHC, J. High Energy Phys. 02 (2018) 083.

[16] A. Abada, N. Bernal, M. Losada, and X. Marcano, Inclusive displaced vertex searches for heavy neutral leptons at the LHC, J. High Energy Phys. 01 (2019) 093.

[17] S. Jana, N. Okada, and D. Raut, Displaced vertex signature of type-I seesaw model, Phys. Rev. D **98**, 035023 (2018).

[18] G. Cottin, J. C. Helo, and M. Hirsch, Displaced vertices as probes of sterile neutrino mixing at the LHC, Phys. Rev. D **98**, 035012 (2018).

[19] J. C. Helo, M. Hirsch, and Z. S. Wang, Heavy neutral fermions at the high-luminosity LHC, J. High Energy Phys. 07 (2018) 056.

[20] E. Accomando, L. Delle Rose, S. Moretti, E. Olaiya, and C. H. Shepherd-Themistocleous, Extra Higgs boson and Z' as portals to signatures of heavy neutrinos at the LHC, J. High Energy Phys. 02 (2018) 109.

[21] F. F. Deppisch, W. Liu, and M. Mitra, Long-lived heavy neutrinos from Higgs decays, J. High Energy Phys. 08 (2018) 181.

[22] A. Das, Pair production of heavy neutrinos in next-to-leading order QCD at the hadron colliders in the inverse seesaw framework, arXiv:1701.04946.

[23] A. Das, N. Okada, and D. Raut, Enhanced pair production of heavy Majorana neutrinos at the LHC, Phys. Rev. D **97**, 115023 (2018).

[24] A. Das, N. Okada, and D. Raut, Heavy Majorana neutrino pair productions at the LHC in minimal U(1) extended Standard Model, Eur. Phys. J. C **78**, 696 (2018).

[25] A. Das, N. Nagata, and N. Okada, Testing the 2-TeV resonance with trileptons, J. High Energy Phys. 03 (2016) 049.

[26] A. Das and N. Okada, Bounds on heavy Majorana neutrinos in type-I seesaw and implications for collider searches, Phys. Lett. B **774**, 32 (2017).

[27] P. S. Bhupal Dev, R. Franceschini, and R. N. Mohapatra, Bounds on TeV Seesaw models from LHC Higgs data, Phys. Rev. D **86**, 093010 (2012).

[28] A. Das, P. S. B. Dev, and C. S. Kim, Constraining sterile neutrinos from precision Higgs data, Phys. Rev. D **95**, 115013 (2017).

[29] A. Das, Y. Gao, and T. Kamon, Heavy neutrino search via the Higgs boson at the LHC, arXiv:1704.00881.

[30] C. Y. Chen, P. S. B. Dev, and R. N. Mohapatra, Probing heavy-light neutrino mixing in left-right seesaw models at the LHC, Phys. Rev. D **88**, 033014 (2013).

[31] P. S. Bhupal Dev, R. N. Mohapatra, and Y. Zhang, Probing TeV scale origin of neutrino mass at lepton colliders, Phys. Rev. D **98**, 075028 (2018).

[32] P. S. B. Dev, R. N. Mohapatra, and Y. Zhang, Lepton Flavor Violation Induced by a Neutral Scalar at Future Lepton Colliders, Phys. Rev. Lett. **120**, 221804 (2018).

[33] C. G. Cely, A. Ibarra, E. Molinaro, and S. T. Petcov, Higgs decays in the low scale type I See-Saw model, Phys. Lett. B **718**, 957 (2013).

[34] A. Ibarra, E. Molinaro, and S. T. Petcov, Low energy signatures of the TeV scale see-saw mechanism, Phys. Rev. D **84**, 013005 (2011).

[35] A. Ibarra, E. Molinaro, and S. T. Petcov, TeV scale see-saw mechanisms of neutrino mass generation, the Majorana nature of the heavy singlet neutrinos and $(\beta\beta)_{0\nu}$-decay, J. High Energy Phys. 09 (2010) 108.

[36] M. Nemevsek, F. Nesti, and G. Popara, Keung-Senjanovic process at the LHC: From lepton number violation to displaced vertices to invisible decays, Phys. Rev. D **97**, 115018 (2018).
[37] M. Nemevsek, F. Nesti, and J. C. Vasquez, Majorana Higgses at colliders, J. High Energy Phys. 04 (2017) 114.
[38] A. Maiezza, M. Nemevsek, and F. Nesti, Lepton Number Violation in Higgs Decay at LHC, Phys. Rev. Lett. **115**, 081802 (2015).
[39] A. Maiezza, M. Nemevsek, and F. Nesti, Perturbativity and mass scales in the minimal left-right symmetric model, Phys. Rev. D **94**, 035008 (2016).
[40] W. Buchmuller and C. Greub, Electroproduction of Majorana neutrinos, Phys. Lett. B **256**, 465 (1991).
[41] W. Buchmuller, C. Greub, and H. G. Kohrs, Effects of heavy majorana neutrinos and neutral vector bosons on electroweak observables, Nucl. Phys. **B370**, 3 (1992).
[42] W. Buchmuller and C. Greub, Right-handed currents and heavy neutrinos in high-energy ep and e^+e^- scattering, Nucl. Phys. **B381**, 109 (1992).
[43] W. Buchmuller, C. Greub, and P. Minkowski, Neutrino masses, neutral vector bosons and the scale of B-L breaking, Phys. Lett. B **267**, 395 (1991).
[44] W. Buchmuller and C. Greub, Heavy Majorana neutrinos in electron-positron and electron-proton collisions, Nucl. Phys. **B363**, 345 (1991).
[45] S. Mondal and S. K. Rai, Probing the heavy neutrinos of inverse seesaw model at the LHeC, Phys. Rev. D **94**, 033008 (2016).
[46] A. Das, P. S. Bhupal Dev, and N. Okada, Direct bounds on electroweak scale pseudo-Dirac neutrinos from $\sqrt{s} =$ 8 TeV LHC data, Phys. Lett. B **735**, 364 (2014).
[47] C. Y. Chen and P. S. B. Dev, Multi-lepton collider signatures of heavy dirac and Majorana neutrinos, Phys. Rev. D **85**, 093018 (2012).
[48] P. S. B. Dev, A. Pilaftsis, and U. k. Yang, New Production Mechanism for Heavy Neutrinos at the LHC, Phys. Rev. Lett. **112**, 081801 (2014).
[49] P. S. B. Dev, D. Kim, and R. N. Mohapatra, Disambiguating seesaw models using invariant mass variables at hadron colliders, J. High Energy Phys. 01 (2016) 118.
[50] S. S. Biswal and P. S. B. Dev, Probing left-right seesaw models using beam polarization at an e^+e^- collider, Phys. Rev. D **95**, 115031 (2017).
[51] A. Das, P. Konar, and S. Majhi, Production of heavy neutrino in next-to-leading order QCD at the LHC and beyond, J. High Energy Phys. 06 (2016) 019.
[52] A. Das and N. Okada, Improved bounds on the heavy neutrino productions at the LHC, Phys. Rev. D **93**, 033003 (2016).
[53] P. S. Bhupal Dev, S. Goswami, M. Mitra, and W. Rodejohann, Constraining neutrino mass from neutrinoless double beta decay, Phys. Rev. D **88**, 091301 (2013).
[54] M. Mitra, G. Senjanovic, and F. Vissani, Neutrinoless double beta decay and heavy sterile neutrinos, Nucl. Phys. **B856**, 26 (2012).
[55] P. S. Bhupal Dev, S. Goswami, and M. Mitra, TeV scale left-right symmetry and large mixing effects in neutrinoless double beta decay, Phys. Rev. D **91**, 113004 (2015).
[56] W. Rodejohann, Neutrinoless double beta decay and neutrino physics, J. Phys. G **39**, 124008 (2012).
[57] H. Pas and W. Rodejohann, Neutrinoless double beta decay, New J. Phys. **17**, 115010 (2015).
[58] M. Gonzlez, M. Hirsch, and S. Kovalenko, Neutrinoless double beta decay and QCD running at low energy scales, Phys. Rev. D **97**, 115005 (2018).
[59] A. Das, P. S. B. Dev, and R. N. Mohapatra, Same sign versus opposite sign dileptons as a probe of low scale seesaw mechanisms, Phys. Rev. D **97**, 015018 (2018).
[60] J. M. Conrad and M. H. Shaevitz, Sterile neutrinos: An introduction to experiments, Adv. Ser. Dir. High Energy Phys. **28**, 391 (2018).
[61] A. Ali, A. V. Borisov, and N. B. Zamorin, Majorana neutrinos and same sign dilepton production at LHC and in rare meson decays, Eur. Phys. J. C **21**, 123 (2001).
[62] S. Mandal and N. Sinha, Favoured B_c decay modes to search for a Majorana neutrino, Phys. Rev. D **94**, 033001 (2016).
[63] S. Mandal, M. Mitra, and N. Sinha, Constraining the right-handed gauge boson mass from lepton number violating meson decays in a low scale left-right model, Phys. Rev. D **96**, 035023 (2017).
[64] M. Lindner, M. Platscher, and F. S. Queiroz, A call for new physics: The muon anomalous magnetic moment and lepton flavor violation, Phys. Rep. **731**, 1 (2018).
[65] A. Abada, C. Biggio, F. Bonnet, M. B. Gavela, and T. Hambye, Low energy effects of neutrino masses, J. High Energy Phys. 12 (2007) 061.
[66] A. Abada, C. Biggio, F. Bonnet, M. B. Gavela, and T. Hambye, mu → e gamma and tau → l gamma decays in the fermion triplet seesaw model, Phys. Rev. D **78**, 033007 (2008).
[67] D. N. Dinh, A. Ibarra, E. Molinaro, and S. T. Petcov, The $\mu - e$ conversion in nuclei, $\mu \to e\gamma$, $\mu \to 3e$ decays and TeV scale see-saw scenarios of neutrino mass generation, J. High Energy Phys. 08 (2012) 125; Erratum, J. High Energy Phys.09 (2013) 23.
[68] S. Antusch and O. Fischer, Non-unitarity of the leptonic mixing matrix: Present bounds and future sensitivities, J. High Energy Phys. 10 (2014) 094.
[69] S. Antusch, C. Biggio, E. Fernandez-Martinez, M. B. Gavela, and J. Lopez-Pavon, Unitarity of the leptonic mixing matrix, J. High Energy Phys. 10 (2006) 084.
[70] M. Blennow, P. Coloma, E. Fernandez-Martinez, J. Hernandez-Garcia, and J. Lopez-Pavon, Non-unitarity, sterile neutrinos, and non-standard neutrino interactions, J. High Energy Phys. 04 (2017) 153.
[71] E. Fernandez-Martinez, J. Hernandez-Garcia, and J. Lopez-Pavon, Global constraints on heavy neutrino mixing, J. High Energy Phys. 08 (2016) 033.
[72] E. Fernandez-Martinez, J. Hernandez-Garcia, J. Lopez-Pavon, and M. Lucente, Loop level constraints on seesaw neutrino mixing, J. High Energy Phys. 10 (2015) 130.
[73] T. Saito *et al.*, Extra dimensions and seesaw neutrinos at the international linear collider, Phys. Rev. D **82**, 093004 (2010).
[74] A. Das and N. Okada, Inverse seesaw neutrino signatures at the LHC and ILC, Phys. Rev. D **88**, 113001 (2013).

[75] S. Banerjee, P. S. B. Dev, A. Ibarra, T. Mandal, and M. Mitra, Prospects of heavy neutrino searches at future lepton colliders, Phys. Rev. D **92**, 075002 (2015).
[76] S. Antusch and O. Fischer, Testing sterile neutrino extensions of the Standard Model at future lepton colliders, J. High Energy Phys. 05 (2015) 053.
[77] R. Talman, Scaling behavior of circular colliders dominated by synchrotron radiation, Int. J. Mod. Phys. A **30**, 1544003 (2015).
[78] S. Antusch, E. Cazzato, and O. Fischer, Higgs production from sterile neutrinos at future lepton colliders, J. High Energy Phys. 04 (2016) 189.
[79] S. Antusch, E. Cazzato, and O. Fischer, Displaced vertex searches for sterile neutrinos at future lepton colliders, J. High Energy Phys. 12 (2016) 007.
[80] S. Antusch, E. Cazzato, and O. Fischer, Sterile neutrino searches at future e^-e^+, pp, and e^-p colliders, Int. J. Mod. Phys. A **32**, 1750078 (2017).
[81] D. Curtin, K. Deshpande, O. Fischer, and J. Zurita, New physics opportunities for long-lived particles at electron-proton colliders, J. High Energy Phys. 07 (2018) 024.
[82] G. Azuelos, M. D'Onofrio, O. Fischer, and J. Zurita, BSM physics at the LHeC and the FCC-he, *Proc. Sci.*, DIS2018 (2018) 190.
[83] J. L. Abelleira Fernandez *et al.* (LHeC Study Group), A large hadron electron collider at CERN: Report on the physics and design concepts for machine and detector, J. Phys. G **39**, 075001 (2012).
[84] M. Lindner, F. S. Queiroz, W. Rodejohann, and C. E. Yaguna, Left-right symmetry and lepton number violation at the large hadron electron collider, J. High Energy Phys. 06 (2016) 140.
[85] G. Azuelos, H. Sun, and K. Wang, Search for singly charged Higgs bosons in vector-boson scattering at ep colliders, Phys. Rev. D **97**, 116005 (2018).
[86] L. Duarte, G. Zapata, and O. A. Sampayo, Angular and polarization trails from effective interactions of Majorana neutrinos at the LHeC, Eur. Phys. J. C **78**, 352 (2018).
[87] S. Mandal, N. Sinha, and M. Mitra, Probing leptoquarks and heavy neutrinos at the LHeC, Phys. Rev. D **98**, 095004 (2018).
[88] A. M. Baldini *et al.* (MEG Collaboration), Search for the lepton flavour violating decay $\mu^+ \to e^+\gamma$ with the full dataset of the MEG experiment, Eur. Phys. J. C **76**, 434 (2016).
[89] B. Aubert *et al.* (*BABAR* Collaboration), Searches for Lepton Flavor Violation in the Decays tau $+ - \to e + -$ gamma and tau $+ - \to$ mu $+ -$ gamma, Phys. Rev. Lett. **104**, 021802 (2010).
[90] B. O'Leary *et al.* (SuperB Collaboration), SuperB progress reports–physics, arXiv:1008.1541.
[91] S. Antusch, E. Cazzato, O. Fischer, A. Hammad, and K. Wang, Lepton flavor violating dilepton dijet signatures from sterile neutrinos at proton colliders, J. High Energy Phys. 10 (2018) 067.
[92] J. A. Casas and A. Ibarra, Oscillating neutrinos and muon $\to$ e, gamma, Nucl. Phys. **B618**, 171 (2001).
[93] S. Antusch and O. Fischer, Probing the nonunitarity of the leptonic mixing matrix at the CEPC, Int. J. Mod. Phys. A **31**, 1644006 (2016).
[94] J. Pumplin, D. R. Stump, J. Huston, H. L. Lai, P. M. Nadolsky, and W. K. Tung, New generation of parton distributions with uncertainties from global QCD analysis, J. High Energy Phys. 07 (2002) 012.
[95] A. Alloul, N. D. Christensen, C. Degrande, C. Duhr, and B. Fuks, FeynRules 2.0—A complete toolbox for tree-level phenomenology, Comput. Phys. Commun. **185**, 2250 (2014).
[96] J. Alwall, R. Frederix, S. Frixione, V. Hirschi, F. Maltoni, O. Mattelaer, H.-S. Shao, T. Stelzer, P. Torrielli, and M. Zaro, The automated computation of tree-level and next-to-leading order differential cross sections, and their matching to parton shower simulations, J. High Energy Phys. 07 (2014) 079.
[97] T. Sjostrand, S. Mrenna, and P. Z. Skands, PYTHIA 6.4 physics and manual, J. High Energy Phys. 05 (2006) 026.
[98] T. Sjöstrand, S. Ask, J. R. Christiansen, R. Corke, N. Desai, P. Ilten, S. Mrenna, S. Prestel, C. O. Rasmussen, and P. Z. Skands, An introduction to PYTHIA 8.2, Comput. Phys. Commun. **191**, 159 (2015).
[99] J. de Favereau, C. Delaere, P. Demin, A. Giammanco, V. Lemaître, A. Mertens, and M. Selvaggi (DELPHES 3 Collaboration), DELPHES 3, A modular framework for fast simulation of a generic collider experiment, J. High Energy Phys. 02 (2014) 057.
[100] Conference talk by O. Fischer, Exotic Higgs Search at Higgs & Top at LHeC, https://indico.cern.ch/event/774889/, LHeC Card for DELPHES is available from https://indico.cern.ch/event/774889/contributions/3220312/attachments/1754841/2845678/delphes\card\LHeC\1.0.tcl.
[101] Y. L. Dokshitzer, G. D. Leder, S. Moretti, and B. R. Webber, Better jet clustering algorithms, J. High Energy Phys. 08 (1997) 001.
[102] M. Wobisch and T. Wengler, Hadronization corrections to jet cross-sections in deep inelastic scattering, In *Hamburg 1998/1999, Monte Carlo generators for HERA physics* 270–279, arXiv:hep-ph/9907280.
[103] M. Cacciari, G. P. Salam, and G. Soyez, FastJet user manual, Eur. Phys. J. C **72**, 1896 (2012).
[104] M. Cacciari and G. P. Salam, Dispelling the N^3 myth for the k_t jet-finder, Phys. Lett. B **641**, 57 (2006).
[105] F. del Aguila, J. de Blas, and M. Perez-Victoria, Effects of new leptons in electroweak precision data, Phys. Rev. D **78**, 013010 (2008).
[106] E. Akhmedov, A. Kartavtsev, M. Lindner, L. Michaels, and J. Smirnov, Improving electro-weak fits with TeV-scale sterile neutrinos, J. High Energy Phys. 05 (2013) 081.
[107] J. de Blas, Electroweak limits on physics beyond the Standard Model, EPJ Web Conf. **60**, 19008 (2013).
[108] P. Achard *et al.* (L3 Collaboration), Search for heavy isosinglet neutrino in e^+e^- annihilation at LEP, Phys. Lett. B **517**, 67 (2001).
[109] M. Agostini *et al.* (GERDA Collaboration), Results on Neutrinoless Double-β Decay of ^{76}Ge from Phase I of the GERDA Experiment, Phys. Rev. Lett. **111**, 122503 (2013).
[110] A. de Gouvea and A. Kobach, Global constraints on a heavy neutrino, Phys. Rev. D **93**, 033005 (2016).
[111] G. Aad *et al.* (ATLAS Collaboration), Search for heavy Majorana neutrinos with the ATLAS detector in pp

collisions at $\sqrt{s} = 8$ TeV, J. High Energy Phys. 07 (2015) 162.

[112] V. Khachatryan *et al.* (CMS Collaboration), Search for heavy Majorana neutrinos in $e^{\pm}e^{\pm} +$ jets and $e^{\pm}\mu^{\pm} +$ jets events in proton-proton collisions at $\sqrt{s} = 8$ TeV, J. High Energy Phys. 04 (2016) 169.

[113] A. M. Sirunyan *et al.* (CMS Collaboration), Search for heavy Majorana neutrinos in same-sign dilepton channels in proton-proton collisions at $\sqrt{s} = 13$ TeV, J. High Energy Phys. 01 (2019) 122.

[114] A. M. Sirunyan *et al.* (CMS Collaboration), Search for heavy neutral leptons in events with three charged leptons in proton-proton collisions at $\sqrt{s} = 13$ TeV, Phys. Rev. Lett. **120**, 221801 (2018).

[115] S. Chakraborty, M. Mitra, and S. Shil, Fat jet signature of a heavy neutrino at lepton collider, arXiv:1810.08970.